In this paper, we report our studies of gene expression changes in B6C3F$_1$ mouse liver induced by multiple doses of two typical alkylating agents, DEN and ENU. We investigated the dose-dependency of gene expression changes at two different time points: 4 h, characterized by the production of many DNA lesions, and 28 days, characterized by fixing of mutations [6]. If we could show dose-dependency in gene expression changes at 4 h, we could clarify key genes related to DNA lesions and subsequent various phenomena in liver cells induced by DEN and ENU. If we could show the dose-dependency in gene expression changes at 28 days, we could clarify key genes related to effects of mutations and subsequent changes that may be causal for carcinogenesis. Our purpose is to determine biological cell responses induced by DEN and ENU by examining the dose-dependency at these two time points.

In addition, we examined gene networks using IPA to elucidate interactions between genes with altered expression.

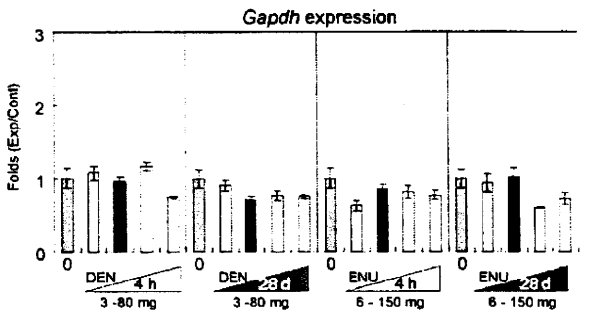

Fig. 1. Relative expression of *Gapdh*. DEN (0–80 mg/kg bw) and ENU (0–150 mg/kg bw) were given to 9-week-old mice (five per group). Total RNA was extracted from pooled liver and reverse-transcribed to cDNA. *Gapdh* expression was determined by qPCR in triplicate assays. Results are shown as mean ± S.D.

2. Materials and methods

2.1. Animal treatment

Male B6C3F$_1$ mice were obtained at 8 weeks of age from Charles River Japan, Inc. (Yokohama, Japan). They were kept in plastic cages on wood chips as bedding and given food (Oriental MF, Oriental Yeast Co., Tokyo) and water *ad libitum* in an air-conditioned room [12 h light (7 a.m. to 7 p.m.), 12 h dark; 23 ± 2 °C; 55 ± 5% humidity]. All animal experiments were conducted in accordance with the NIH Guide for Care and Use of Laboratory Animals and approved by the Animal Care and Use Committee at the Mitsubishi Chemical Safety Institute Ltd.

Mice at 9 weeks of age were injected intraperitoneally (i.p.) with DEN (3, 9, 27 and 80 mg/kg bw; Wako Pure Chem. Ind. Ltd., Osaka, Japan; CAS 55-18-5) dissolved in sterile water or ENU (6, 17, 50 and 150 mg/kg bw; Wako Pure Chem. Ind. Ltd., Osaka, Japan; CAS 759-73-9) dissolved in sterile water. Control animals for the DEN- and ENU-treated groups received sterile water. At 4 h and 28 days after treatment, animals were sacrificed after which the liver was collected, frozen on dry ice, and stored at −80 °C until use.

2.2. RNA isolation and relative quantification by real-time PCR

To isolate total RNA, approximately 150 mg from each liver (main lobe) was placed into TRIzol reagent (Invitrogen Corp., Carlsbad, CA, USA) and immediately homogenized using a Potter homogenizer. The samples were further homogenized with a 1 ml syringe and 18 gauge needle. Finally, total RNA was purified using an ethanol precipitation method. Complementary DNA (cDNA) was yielded from total RNA using the SuperScript First strand synthesis system for RT-PCR kit (Invitrogen Corp.).

qPCR amplifications were performed in triplicate using the SYBR Green I assay in an Opticon II (MJ Research, Inc., Waltham, MA, USA). The reactions were carried out in a 96-well plate in 20-μl reactions containing 2 × SYBR Green Master Mix (Applied Biosystems, Lincoln Centre Drive Foster City, CA, USA), 2 pmol each of forward and reverse primer, and a cDNA template corresponding to 10 ng total RNA. Each primer sequence and Ct value are shown in Table 2. We selected 51 genes based on our previous results from the original DNA microarray and Affymetrix GeneChip Mu74AV2 for samples after treatment of DEN, dimethylnitrosamine, dipropylnitrosamine, ENU, *o*-aminoazotoluene, 7,12-dimethylbenz[*a*]anthracene, dibenzo[*a*,*l*]pyrene, phenobarbital and ethanol in our JEMS/MMS/Toxicogenomics group collaborative study. *Gapdh* and *Hprt1* were selected as housekeeping genes. SYBR Green PCR conditions were 95 °C for 10 min, followed by 95 °C for 10 s, 58 °C for 50 s and 72 °C for 20 s, for 45 cycles. In each assay a standard curve was determined concurrently with examined samples. In the preliminary experiment the highest group was selected for each gene and was used as the standard sample in the subsequent assay. In each standard curve determination, there were six dilution series of standard samples, diluted up to 1/5, 1/25, 1/125, 1/625 and 1/3125 of the selected standard liver cDNA for each gene. Finally, relative quantitative values of each sample were determined with 1/25 diluted cDNA and were normalized with those of the *Gapdh* genes. Relative *Gapdh* expression levels of experimental groups are presented in Fig. 1.

2.3. Data analysis and clustering algorithm

For the cluster analysis program, we performed a logarithmic ($\log_2$) transformation of the data to stabilize the variance and the gene expression profile of each DEN- and ENU-treated sample, normalized to the median gene expression level for the entire sample set. Both hierarchical and *k*-means clustering were performed using GENESIS software (http://genome.tugraz.at/) [13] for each data set at 4 h and 28 days separately. Gene groups were presented automatically by hierarchical clustering. Four clusters were set up initially in *k*-means clustering based on hierarchical clustering results. Genes which belonged to dose–response groups by both clustering methods were defined as dose–response genes. Furthermore, genes which showed less than a 0.5-fold decrease dose-dependently were evaluated as decrease genes by expression pattern because the decrease genes were few and could not be extracted using both clustering methods.

The color displays given in Fig. 2 show the $\log_2$ (expression ratio) as (1) red when the treatment sample is up-regulated relative to the control sample, (2) blue when the treatment sample is down-regulated relative to the control sample and (3) white when the $\log_2$ (expression ratio) is close to zero.

2.4. Pathway analysis

Numerical experimental data at 4 h and 28 days after DEN or ENU treatment were separately analyzed by ingenuity pathway analysis (IPA) Software-Complete Pathways Database. These data were generated through the use of IPA, a web-delivered application (www.Ingenuity.com) that enables the visualization and analysis of biologically relevant networks to discover, visualize, and explore therapeutically relevant networks. IPA information was extracted by experts from the full text of the scientific literature, including information about genes, drugs, chemicals, cellular and disease processes, and signaling and metabolic pathways.

Expression data sets containing gene identifiers (Entrez gene identifiers) and their corresponding expression values as fold changes were uploaded as a tab-delimited text file. Each gene identifier was mapped to its corresponding gene object in the Ingenuity Pathways Knowledge Base. To start building networks, the application program queries the Ingenuity Pathways Knowledge Base for interactions between focus genes and all other gene objects stored in the knowledge base and generates a set of networks. The program then computes a score for each network according to the fit of the network to the set of focus genes. The score indicates the likelihood of the focus genes in a given network being found together due to random chance. A score of >2 indicates that there is a <1 in 100 chance that the focus genes were assembled randomly into a network due to random chance.

3. Results

3.1. Dose-dependent alteration of gene expression induced by DEN

3.1.1. Clustering analysis for gene expression

Unsupervised hierarchical clustering results are shown in Fig. 2. The changes in gene expression are represented colorimetrically as described in Section 2. The clustering presented four groups (DEN-4 h-Grp-1 to DEN-4 h-Grp-4) and an ungrouped gene 4 h after administration, and three groups (DEN-28 d-Grp-1 to DEN-28 d-Grp-3) and eight ungrouped genes 28 days after administration. As unsupervised hierarchical clustering was performed for 4 h and 28-day samples separately, group member genes were different for 4 h groups and 28-day groups.

At 4 h, all 20 DEN-4 h-Grp-1 genes showed a dose-dependent increase of more than 3–64-fold. Twelve DEN-4 h-Grp-2 genes were suggested to have a gradual dose-dependent increase of less than that for the expression in DEN-4 h-Grp-1. Two DEN-4 h-Grp-4 genes exhibited a dose-dependent decrease of less than 0.3-fold.

Table 2
Primer sequences of 51 genes examined in the study.

No.	Symbol	Left	Right	Ct
1	*Bax*	CCAGGATGCGTCCACCAAGAAG	GGAGTCCGTGTCCACGTCAGC	28
2	*Bcl2*	GATGACTTCTCTCGTCGCTACC	CATCCCTGAAGAGTTCCTCCAC	31
3	*Btg2*	ACGGGAAGAGAACCGACATGC	ATGATCGGTCAGTGCGTCCTG	24
4	*Casp1*	GTCTTGGAGACATCCTGTCAGG	GCATCTGTAGCCTAAATTCTGG	32
5	*Ccnf*	AGCACAAAGCCTTGCCACCATC	AAGCCAGGTGCGTGTCCTTGTC	25
6	*Ccng1*	TGGCCGAGATTTGACCTTCTGG	GTGCTTCAGTTGCCGTGCAGTG	22
7	*Ccng2*	GCCATCAAGCTAGGACTGTTAG	CACTTATCAACTCCATTCCCTG	26
8	*Cdkn1a (p21)*	TCCCGTGGACAGTGAGCAGTTG	CGTCTCCGTGACGAAGTCAAAG	22
9	*Cyp1a1*	TGGCCGATCGGAGGTCTTTC	AAGTGTTCACAGCGGGCGTG	29
10	*Cyp1a2*	GATGCTCTTCGGCTTGGGAAAG	CCATAGTTGGGTGTCAGGTCCAC	20
11	*Cyp4a10*	AGCCACAAGGGCAGTGTTCAGG	CCAAGCCGCCATTGGAAGAAAG	23
12	*Cyp21a1*	TGTGCTGCCCTTAAAGAAGAGTG	TTGAGCATCCCGTTCCCGTTTC	25
13	*Dpyd*	GTGCGGCTAAAGGCTGATGTGG	CCCATGGTTCACTGGTTTGCATG	24
14	*Egfr*	AGAACGCCTTCCACAGCCAC	ACTCTCGGAACTTTGGGCGG	22
15	*Ephx1*	CATTGTCTCCTCCCAGCGCTTC	GGGCATGCAGGATCTCAGAAGG	21
16	*Fabp5*	ACGGTCTGCACCTTCCAAGACG	ACCCGAGTGCAGGTGGCATTG	24
17	*Fos*	GTCGACCTAGGGAGGACCTTAC	CATCTCTGGAAGAGGTGAGGAC	31
18	*Gadd45b*	TGTACGAGGCGGCCAAACTG	TGTCGCAGCAGAACGACTGG	28
19	*Gadd45g*	GGAAAGCACAGCCAGGATGCAG	ATTCAGGACTTTGGCGGACTCG	26
20	*Gapdh*	GCTCTCAATGACAACTTTGTCAAG	CTTCCTTGGAGGCCATGTAGGC	22
21	*Gdf15*	AGCTGGAACTGCGCTTACGGG	CTCCAGCCCAAGTCTTCAAGAG	28
22	*Glul*	GGAATGGAGCAGGAATATACTC	ACCCCAGTAATACGGGCCTTG	22
23	*Gstk1*	CGTACTCCTGGCTGGGGCTTTG	CAGGTGGTTGGTTGCCGCTGTC	24
24	*Gyk*	GCCTGAAACAACTGCACTAGGC	CACAGCTTTCTTCCATGTGGAG	27
25	*Hist1h1c*	CGAGCTCATCACCAAGGCTGTG	CCCTTGCTCACCAGGCTCTTC	26
26	*Hspa1b (Hsp70)*	GACAAGTCGGAGAACGTGCAG	CGAGTAGGTGGTGAAGGTCTG	25
27	*Hspb1*	CGGTGCTTCACCCGGAAATAC	GCTGACTCCGTGACTGCTTTCG	25
28	*Hspb2 (Hsp27)*	CTCACAGTGAAGACCAAGGAAG	GGATAGGGAAGAGGACACTAGG	26
29	*Hmox1*	AAGACCGCCTTCCTGCTCAAC	CGAAGTGACGCCATCTGTGAGG	28
30	*Hprt1*	CTTGCTCGAGATGTCATGAAGGAG	TAATCCAGCAGGTCAGCAAAGAAC	26
31	*Igfbp1*	GATCAGCCCATCCTGTGGAACG	TTCTCGTTGGCAGGGCTCCTTC	24
32	*Isg20l1*	TTGAAGGGCAAGGTGGTGGTG	GAGCAGGTTTGGGACATAAGTG	24
33	*Jun*	GCCAAGAACTCGGACCTTCTC	AGTGGTGATGTGCCCATTGCTG	23
34	*Kras*	GGCAAGAGCGCCTTGACGATAC	TGGTCCCTCATTGCACTGTACTCC	28
35	*Lig3*	TGCGGCTCTACTTGCCACCTTC	CATGTGTGGCTGAGCCCATGTC	27
36	*Lrp1*	GGGCCATGAATGTGGAAATTGG	GTGGCATACACTGGGTTGGTG	22
37	*Mbd1*	GGATCCTGACACTCAAGAATGG	GTTTGGGCTAACACAGGAAGAG	23
38	*Mdm2*	TTGATCCGAGCCTGGGTCTGTG	AAGATCCTGATGCGAGGGCGTC	27
39	*Myc*	B5,6TCAGCAACAACCGCAAGTGCTC	AAAGCTGCGCTTCAGCTCGTTC	32
40	*Net1*	GACCTCCACGAAGAGTGTGAAG	CTGTACACTGGAGCCACAATCC	27
41	*Pdgfb*	AAGACGCGCACAGAGGTGTTCC	GGCATTGCACATTGCGGTTATTG	33
42	*Plk2*	CTGTTGAGAGCGTCTTCAGTTG	CCATAGTTCACAGTTAAGCAGC	28
43	*Pml*	GGCAAGAAGCGTCCTTACCTTC	GGACAGCAACAGCAGTTCAGTC	28
44	*Pmm1*	TGTCCCGAGGAGGCATGATAAG	CAAAGTCATTCCCGCCAGGAC	30
45	*Ppp1r3c*	TGGAAACCTGACGGAGTGCAG	GCAAGCCTTGGACTGCCAAAG	24
46	*Rad52*	TGACGCCACTCACCAGAGGAAG	GCTGGAAGTACCGCATGCTTGG	30
47	*Rcan1*	GGTCCACGTGTGTGAGAGTG	TGGATGGGTGTGTACTCCGG	24
48	*Trp53*	TTGGACCCTGGCACCTACAATG	GCAGACAGGCTTTGCAGAATGG	26
49	*Tubb2c*	TTGGCAACAGCACCGCTATTC	TCGGACACCAGGTCGTTCATG	23
50	*Ube2e1 (UbcM3)*	AACTGGAGCCCAGCCCTAACC	TGGCCATTCTGTCGTGTTCTGC	24
51	*Ung*	AACCTGAGTGGCCTCGTCTTCC	TCTGCATCCCAGGAACCCTCTG	29

Ct values are those of the highest group in the present experimental condition.

At 28 days, three DEN-28 d-Grp-1 genes showed a dose-dependent increase of more than four-fold. Seventeen DEN-28 d-Grp-2 genes were suggested to have a gradual dose-dependent increase, though less than that for the expression in DEN-28 d-Grp-1. Ungrouped *Igfbp1* showed a dose-dependent decrease of less than 0.3-fold.

Unsupervised *k*-means clustering results are shown in Fig. 3A. Genes were classified into four clusters based on the hierarchical clustering results. Gene expression was classified into four clusters (DEN-4 h-Cluster-1 to DEN-4 h-Cluster-4) 4 h after administration, and four clusters (DEN-28 d-Cluster-1 to DEN-28 d-Cluster-4) 28 days after administration. As unsupervised *k*-means clustering was performed for 4 h and 28-day data separately, cluster member genes were different for 4 h and 28 days.

At 4 h, all 12 DEN-4 h-Cluster-1 genes exhibited a dose-dependent increase of more than eight-fold. Fourteen DEN-4 h-Cluster-2 genes showed a gradual dose-dependent increase as compared to DEN-4 h-Cluster-1 genes. Although *Myc* and *Igfbp1* in DEN-4 h-Cluster-3 had some atypical dose-response, they showed an increase of up to or greater than two-fold, as a whole. Two genes in DEN-4 h-Cluster-4 exhibited a dose-dependent decrease of less than 0.3-fold [*Cyp1a2* and *Glul*]. For 28-day data, 4 DEN-28 d-Cluster-1 genes showed a dose-dependent increase of more than two-fold. *Igfbp1* in DEN-28 d-Cluster-3 showed a dose-dependent decrease of less than 0.3-fold.

Two types of clustering results for the DEN data are summarized as follows. A total of 28 genes showed a dose-dependent increase or decrease at 4 h or 28 days after administration. Twenty-six genes in DEN-4 h-Grp-1 or DEN-4 h-Grp-2 and DEN-4 h-Cluster-1, DEN-4 h-Cluster-2 or DEN-4 h-Cluster-3 showed a dose-dependent increase ranging from 2-fold to more than 64-fold [*Bax*, *Btg2*, *Ccng1*, *Ccng2*, *Cdkn1a*, *Cyp4a10*, *Cyp21a1*, *Fos*, *Gadd45b*, *Gdf15*, *Hspb1*, *Hmox1*, *Hsp27*, *Igfbp1*, *Isg20l1*, *Jun*, *Mbd1*, *Mdm2*, *Myc*, *Net1*, *Plk2*, *Pmm1*, *Ppp1r3c*, *Rad52*, *Rcan1* and *Tubb2c*]. Two genes in DEN-4 h-Grp-4

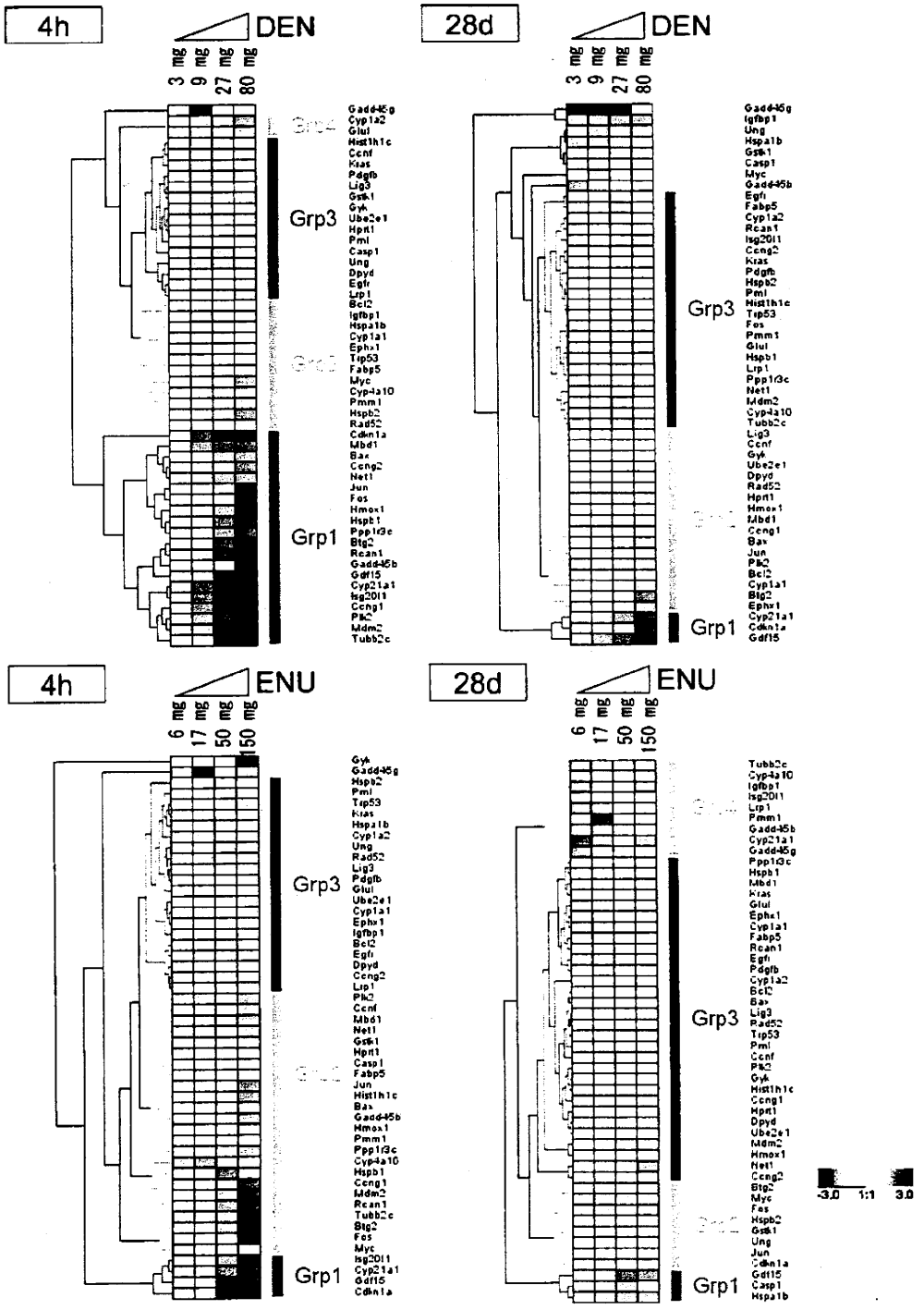

Fig. 2. Cluster analysis of gene expression after DEN and ENU treatment. The expression of 50 genes was clustered by hierarchical clustering after DEN or ENU treatment. Results of 4 h and 28 days were analyzed separately. The color displays show the $\log_2$ (expression ratio) as (1) red when the treatment sample is up-regulated relative to the control sample, (2) blue when the treatment sample is down-regulated relative to the control sample and (3) white when the $\log_2$ (expression ratio) is close to zero.

and DEN-4 h-Cluster-4 showed a dose-dependent decrease of less than 0.3-fold [*Cyp1a2* and *Glul*].

At 28 days, four genes in DEN-28 d-Grp-1 or DEN-28 d-Grp-2 and DEN-28 d-Cluster-1, which showed a dose-dependent increase at 4 h, also showed a dose-dependent increase by more than 2–4-fold [*Btg2*, *Cdkn1a*, *Cyp21a1* and *Gdf15*]. *Igfbp1* in the ungrouped group and DEN-28 d-Cluster-3 showed a dose-dependent decrease of less than 0.3-fold.

3.1.2. Identification of biologically relevant networks for DEN treatment

DEN numerical data of all 51 examined genes were analyzed by IPA, and 5 gene networks were extracted (Table 3). Five networks are also shown as bar graphs in Fig. 4.

For the 4 h time point, 35 genes were extracted in DEN-4 h-Network-1 (cancer, cell cycle and reproductive system disease); of these, 15 genes were examined in this study, and 11 of these genes showed a dose-dependent response [*Bax*, *Btg2*, *Ccng1*, *Cdkn1a*, *Gadd45b*, *Gdf15*, *Hspb1*, *Hspb2*, *Mdm2*, *Plk2* and *Pmm1*] (Fig. 4A, Network-1). Network-1 was a highly active network for DEN-4 h. *Trp53* and *Cdkn1a* appeared to be core genes in DEN-4 h-Network-1. *Trp53* has 15 associations [*Bax*, *Btg2*, *Casp1*, *Ccng1*, *Cdkn1a*, *Gadd45 complex*, *Gdf15*, *Hist1h1c*, *Hspb1*, *Mdm2*, *Plk2*, *Pml*, *Pmm1*, *Pdgf* complex and *Caspase* complex], and *Cdkn1a* has 9 associations [*Trp53*, *Plk2*, *Pdgf complex*, *Gdf15*, *Gadd45b*, *Gadd45g*, *Mdm2*, *Caspase* complex and *Pml*].

DEN-4 h-Network-2 (cell cycle, DNA replication, recombination, repair and cell death) consisted of 35 genes, 15 of which were examined in this study; 11 of these genes showed a dose-dependent

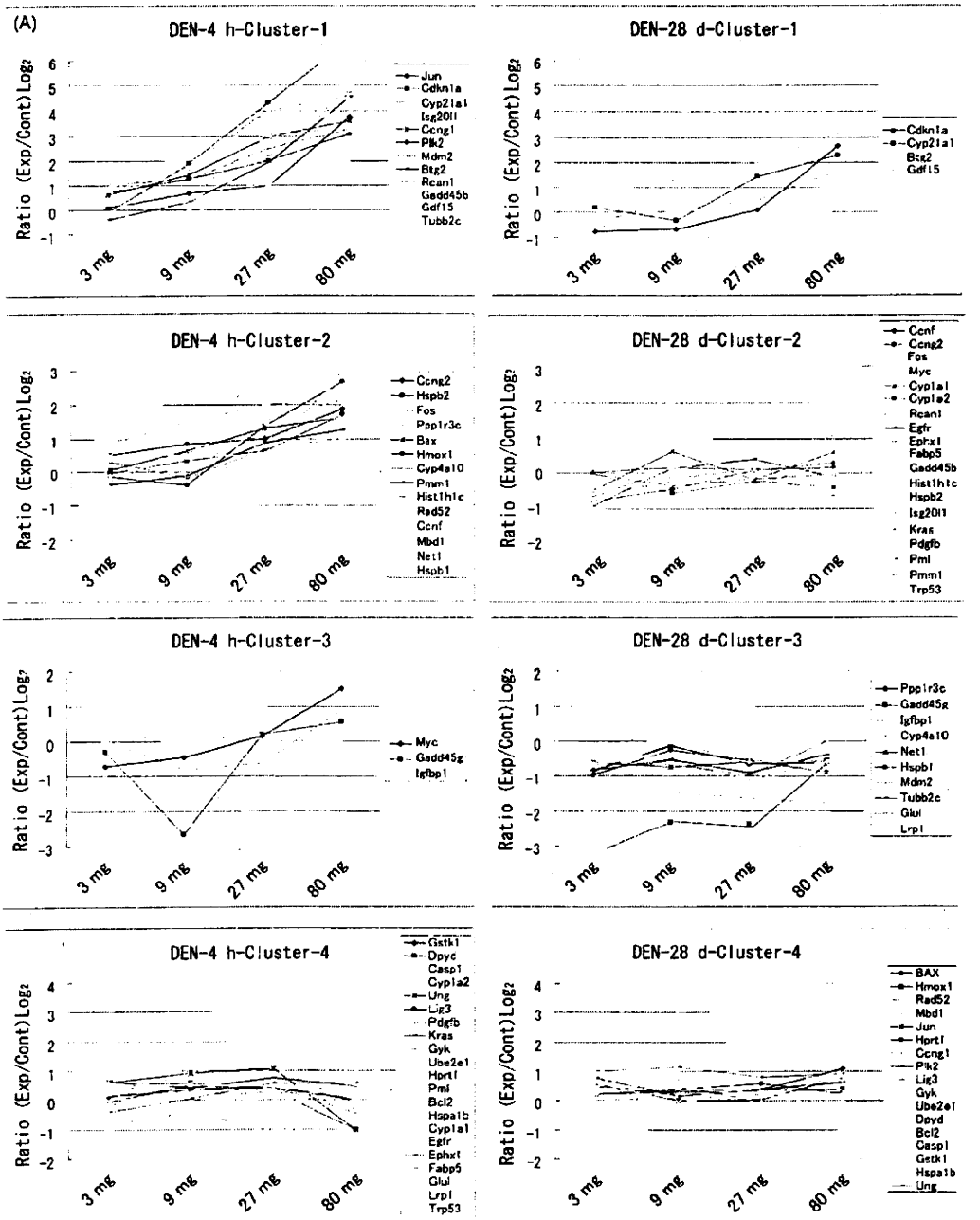

Fig. 3. Cluster analysis and dose-dependent expression pattern. The expression of 50 genes was clustered by *k*-means clustering after (A) DEN or (B) ENU treatment. Results of 4 h and 28 days were analyzed separately.

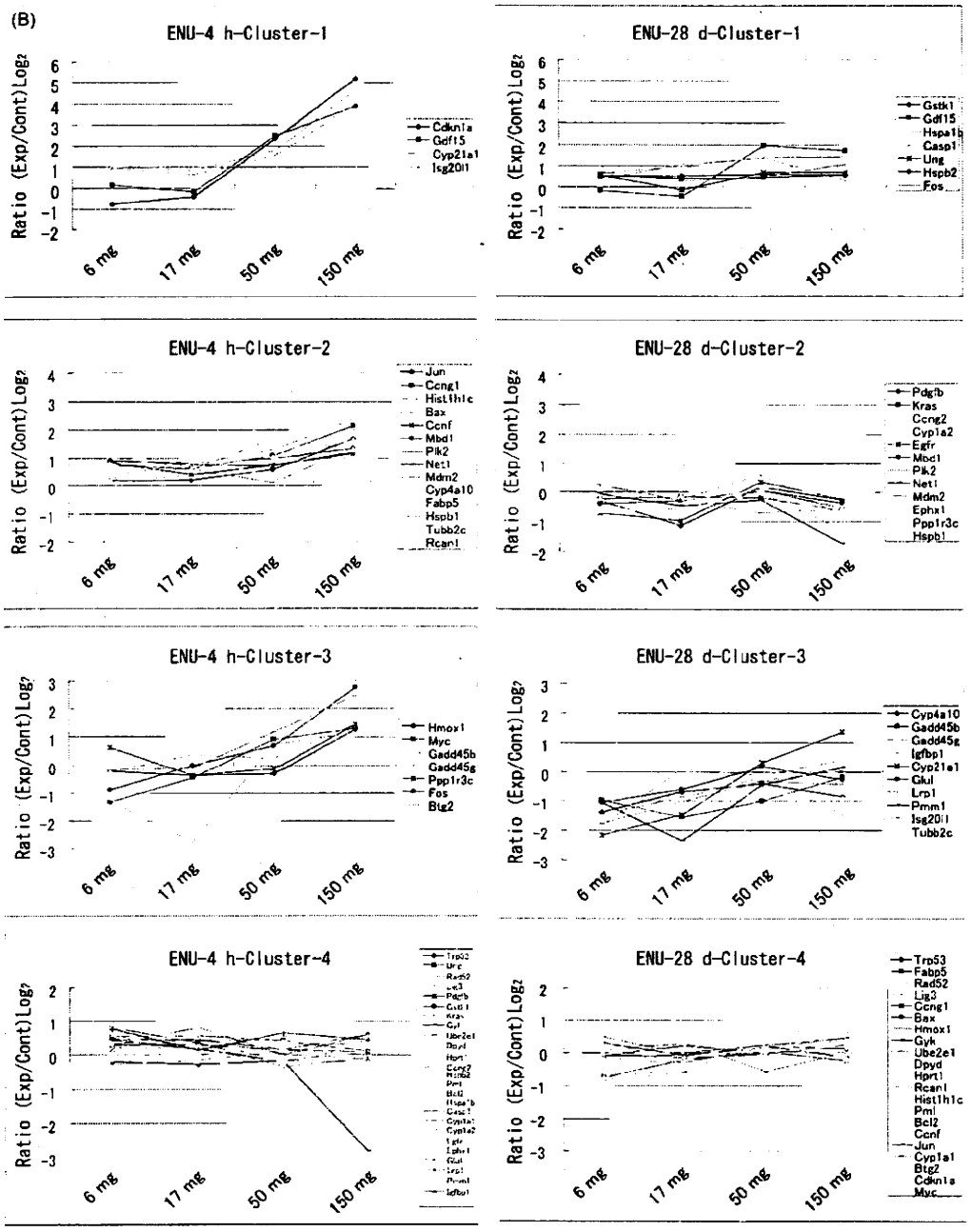

Fig. 3. (*Continued*).

response [*Ccng2*, *Cyp1a2*, *Cyp4a10*, *Cyp21a1*, *Gdf15*, *Glul*, *Igfbp1*, *Ppp1r3c Rad52*, *Rcan1* and *Tubb2c*] (Fig. 4A, Network-2). Network-2 was also a highly active network for DEN-4 h. *Il1b* and *Sp1* seemed to be core genes in DEN-4 h-Network-2. *Il1b* has five associations [*Gdf15*, *Fabp5*, *Rcan1*, *Igfbp1* and *Hprt1*], and *Sp1* has three associations [*Gdf15*, *Igfbp1* and *Cyp21a1*].

DEN-4 h-Network-3 (liver necrosis/cell death and hepatic system disease) consisted of 36 genes, 10 of which were examined in this study; 5 of these genes showed a dose-dependent response [*Fos*, *Hmox1*, *Jun*, *Myc* and *Net1*) (Fig. 4A, Network-3).

DEN-4 h-Network-4 (cell cycle, DNA replication, recombination, repair and cell death) consisted of 35 genes, 9 of which were examined in this study; 2 of these genes [*Isg20l1* and *Mbd1*] showed a dose-dependent response (Fig. 4A, Network-4).

DEN-4 h-Network-5 (cancer, drug metabolism and genetic disorder) consisted of two genes, neither of which showed a dose-dependent response in this study (Fig. 4A, Network-5).

For 28-day data, DEN-28 d-Network-1 consisted of the same genes and the same top functions as for DEN-4 h-Network-1 (Table 3(B)); however, a generally lower dose-dependent response

Table 3
Gene networks and their primary functions after DEN and ENU treatment.

Networks	Molecules in network	Top functions
(A) DEN 4 h		
1	Adaptor protein 2, Ahr-aryl hydrocarbon-*Arnt*, *Arf*, ***Bax***, ***Btg2***, *Casp1*, Caspase, *Cbp/p300*, ***Ccng1***, ***Cdkn1a***, *Creb*, Cyclin A, Cyclin E, *E2f*, *Erk1/2*, *Gadd45*, ***Gadd45b***, *Gadd45g*, ***Gdf15***, *Gsk3*, *Hist1h1c*, ***Hspb1***, ***Hspb2***, *Jun/Junb/Jund*, ***Mdm2***, *Mek1/2*, *Pak*, *Pdgf*, ***Plk2***, *Pml*, ***Pmm1***, *Pp2a*, *Rb*, *Stat*, *Trp53*	Cancer, Cell cycle, reproductive system disease
2	*Aatf*, *Aldh3a1*, *App*, beta-estradiol, *Ccne2*, ***Ccng2***, ***Cyp1a2***, ***Cpy21a1***, ***Cyp4a10***, *E2F1*, *Fabp5*, ***Gdf15***, *Gyk*, ***Glul***, *Hprt1*, *Hspa1b*, ***Igfbp1***, *Igfbp7*, *Il10*, *Il1b*, *Irf2*, *Klf10*, *MAZ*, *Meis1*, *Muc2*, ***Ppp1r3c***, ***Rad52***, ***Rcan1***, retinoic acid, *Scye1*, *Sp1*, *St8sia1*, *Tgm1*, *TopbpP1*, ***Tubb2c***	Cell cycle, DNA replication, recombination, and repair, cell death
3	*Akt*, *Ap1*, *Bcl2*, Calpain, *Egfr*, *Fgf*, ***Fos***, *Fos-Jun*, ***Hmox1***, *Ige*, *Il1*, *Jnk*, ***Jun***, *Kras*, *Lig3*, *Mapk*, *Mek*, *Mmp*, ***Myc***, ***Net1***, *P38*, *Mapk*, *Pdgf bb*, *Pdgfb*, *Pi3k*, *Pkc(s)*, *Pkg*, *Rar*, *Ras*, *Ras* homolog, *Rock*, *Rxr*, *Sos*, *Stat5a/b*, *Tgf* beta, *Vegf*	Cell death, hepatic system disease, liver necrosis/cell death
4	4-Phenylbutyric acid, *14-3-3*, Calmodulin, *Ccnf*, *Cdkn2a*, *Ck2*, *Cul1*, Cyclin D, *Cyp1a1*, *Ephx1*, *Hira*, Histone h3, *Hnrpa2b1*, *Hsp70*, *Hsp90*, *Hspa1b*, hydrogen peroxide, *Ifng*, *Irf2*, ***Isg20l1***, lipoxin A4, *Lrp1*, ***Mbd1***, *Mcm2*, *Mcm3*, *Meis1*, *Pdk1*, *Pka*, RNA polymerase II, *Ssrp1*, *Supt16h*, *Tp53inp1*, *Ube2e1*, Ubiquitin, *Ung*	Cell cycle, DNA replication, recombination, and repair, cell death
5	*Cdh3*, D *Dpyd*	Cancer, drug metabolism, genetic disorder
(B) DEN 28 d		
1	Adaptor protein 2, Ahr-aryl hydrocarbon-*Arnt*, *Arf*, *Bax*, ***Btg2***, *Casp1*, Caspase, *Cbp/p300*, *Ccng1*, ***Cdkn1a***, *Creb*, Cyclin A, Cyclin E, *E2f*, *Erk1/2*, *Gadd45*, *Gadd45b*, *Gadd45g*, ***Gdf15***, *Gsk3*, *Hist1h1c*, *Hspb1*, *Hspb2*, *Jun/Junb/Jund*, *Mdm2*, *Mek1/2*, *Pak*, *Pdgf*, *Plk2*, *Pml*, *Pmm1*, *Pp2a*, *Rb*, *Stat*, *Trp53*	Cancer, cell cycle, reproductive system disease
2	*Aatf*, *Aldh3a1*, *App*, beta-estradiol, *Ccng2*, *Cyp1a2*, ***Cyp21a1***, *Cyp4a10* (includes EG:1579), *E2f1*, *Fabp5*, ***Gdf15***, *Gyk*, *Glul*, *Hrpt1*, *Hspa1b*, ***Igfbp1***, *Il10*, *Il1b*, *Klf10*, *Klk5*, *Maz*, *Meis1*, *Mt1e*, *Muc2*, *Nr4a3*, *Ppp1r3c*, *Rad52*, *Rcan1*, retinoic acid, *Scye1*, *Sp1*, *St8sia1*, *Tgm1*, *Topbp1*, *Tubb2c*	DNA replication, recombination, and repair, cell death, cell cycle
3	*Akt*, *Ap1*, *Bcl2*, Calpain, *Egfr*, *Fgf*, *Fos*, *Fos-Jun*, *Hmox1*, *Ige*, *Il1*, *Jnk*, *Jun*, *Kras*, *Lig3*, *Mapk*, *Mek*, *Mmp*, *Myc*, *Net1*, *P38 Mapk*, *Pdgf bb*, *Pdgfb*, *Pi3k*, *Pkc(s)*, *Pkg*, *Rar*, *Ras*, *Ras* homolog, *Rock*, *Rxr*, *Sos*, *Stat5a/b*, *Tgf* beta, *Vegf*	Cell death, hepatic system disease, liver necrosis/cell death
4	*14-3-3*, *Bag4*, Calmodulin, *Ccnf*, *Cdkn2a*, *Ck2*, *Cul1*, *Cyp1a1*, *Dynlrb1*, *Ephx1*, *Hira*, Histone h3, *Hnrpa2b1*, *Hoxb9*, *Hsp70*, *Hsp90*, *Hspa1b*, hydrogen peroxide, *Ifng*, *Isg20l1*, *Lrp1*, *Mbd1*, *Meis1*, *Nol3*, *Pdk1*, *Pka*, *Ppfibp1*, RNA pol2-transcription factor, RNA polymerase II, *Smtn*, *Supt16h*, *Tp53inp1*, *Ube2e1*, Ubiquitin, *Ung*	Cellular development, cellular growth and proliferation, connective tissue development and function
5	*Cdh3*, *Dpyd*	Cancer, drug metabolism, genetic disorder
(C) ENU 4 h		
1	Adaptor protein 2, Ahr-aryl hydrocarbon-*Arnt*, *Arf*, ***Bax***, ***Btg2***, *Casp1*, Caspase, *Cbp/p300*, ***Ccng1***, ***Cdkn1a***, *Creb*, Cyclin A, Cyclin E, *E2f*, *Erk1/2*, *Gadd45*, ***Gadd45b***, *Gadd45g*, ***Gdf15***, *Gsk3*, ***Hist1h1c***, ***Hspb1***, *Hspb2*, *Jun/Junb/Jund*, ***Mdm2***, *Mek1/2*, *Pak*, *Pdgf*, ***Plk2***, *Pml*, *Pmm1*, *Pp2a*, *Rb*, *Stat*, *Trp53*	Cancer, cell cycle, reproductive system disease
2	*Aatf*, *Aldh3a1*, *App*, *Apphp1*, beta-estradiol, *Ccne2*, *Ccng2*, *Cyp1a2*, ***Cyp21a1***, ***Cyp4a10***, *E2f1*, ***Fabp5***, ***Gdf15***, *Gyk*, *Glul*, *Hprt1*, *Hdps1b*, *Igfbp1*, *Il10*, *Il1b*, *Klf10*, *Maz*, *Mis1*, *Muc2*, *Nr4a3*, ***Ppp1r3c***, *Rad52*, ***Rcan1***, retinoic acid, *Scye1*, *Sp1*, *St8sia1*, *Tgm1*, *Tophp1*, ***Tubb2c***	DNA replication, recombination, and repair, cell cycle, cell signaling
3	*Akt*, *Ap1*, *Bcl2*, Calpain, *Egfr*, *Fgf*, ***Fos***, *Fos-Jun*, ***Hmox1***, *Ige*, *IL1*, *Jnk*, ***Jun***, *Kras*, *Lig3*, *Mapk*, *Mek*, *Mmp*, ***Myc***, ***Net1***, *P38*, *Mapk*, *Pdgf bb*, *Pdgfb*, *Pi3k*, *Pkc(s)*, *Pkg*, *Rar*, *Ras*, *Ras* homolog, *Rock*, *Rxr*, *Sos*, *Stat5a/b*, *Tgf* beta, *Vegf*	Cell death, hepatic system disease, liver necrosis/cell death
4	4-phenylbutyric acid, *14-3-3*, Calmodulin, ***Ccnf***, *Cdkn2a*, *Ck2*, *Cul1*, Cyclin D, *Cyp1a1*, *Ephx1*, *Hira*, Histone h3, *Hnrpa2b1*, *Hsp70*, *Hsp90*, *Hspa1b*, hydrogen peroxide, *Ifng*, *Irf2*, ***Isg20l1***, lipoxin A4, *Lrp1*, ***Mbd1***, *Mcm2*, *Mcm3*, *Meis1*, *Pdk1*, *Pka*, RNA polymerase II, *Ssrp1*, *Supt16h*, *Tp53inp1*, *Ube2e1*, Ubiquitin, *Ung*	Cell cycle, DNA replication, recombination, and repair, cell death
5	*Cdh3*, *Dpyd*	Cancer, drug metabolism, genetic disorder
(D) ENU 28 d		
1	Adaptor protein 2, Ahr-aryl hydrocarbon-*Arnt*, *Arf*, *Bax*, *Btg2*, ***Casp1***, Caspase, *Cbp/p300*, *Ccng1*, *Cdkn1a*, *Creb*, Cyclin A, Cyclin E, *E2f*, *Erk1/2*, *Gadd45*, *Gadd45b*, *Gadd45g*, ***Gdf15***, *Gsk3*, *Hist1h1c*, *Hspb1*, ***Hspb2***, *Jun/Junb/Jund*, *Mdm2*, *Mek1/2*, *Pak*, *Pdgf*, *Plk2*, *Pml*, *Pmm1*, *Pp2a*, *Rb*, *Stat*, *Trp53*	Cancer, cell cycle, reproductive system disease
2	*Aatf*, Ahr-aryl hydrocarbon, *App*, *Apphp1*, beta-estradiol, *Ccng2*, *Cd68*, *Cdc45l*, *Cyp1a2*, *Cyp21a1*, *Cyp4a10*, *E2f1*, *Fabp5*, *Folr2*, ***Gdf15***, *Gyk*, *Glul*, *Hprt1*, ***Hspa1b***, *Igfbp1*, *Il10*, *Il1b*, *Klk5*, *Krt16*, *Nr4a3*, *Ppp1r3c*, *Rad52*, *Rcan1*, retinoic acid, *Rrs4x*, *Serpinb9*, *Sp1*, *TacstdA1*, *Tspo*, *Tubb2c*	Cell signaling, molecular transport, small molecule biochemistry
3	*Akt*, *Ap1*, *Bcl2*, Calpain, *Egfr*, *Fgf*, ***Fos***, *Fos-Jun*, *Hmox1*, *Ige*, *IL1*, *Jnk*, *Jun*, *Kras*, *Lig3*, *Mapk*, *Mek*, *Mmp*, *Myc*, ***Net1***, *P38*, *Mapk*, *Pdgf bb*, *Pdgfb*, *Pi3k*, *Pkc(s)*, *Pkg*, *Rar*, *Ras*, *Ras* homolog, *Rock*, *Rxr*, *Sos*, *Stat5a/b*, *Tgf* beta, *Vegf*	Cell death, hepatic system disease, liver necrosis/cell death
4	*14-3-3*, *Aco1*, *Asf1b*, *Bag4*, Calmodulin, *Ccnf*, *Cdkn2a*, *Ck2*, *Cyp1a1*, *Dynlrb1*, *Ephx1*, *Hira*, Histone h3, *Hosb9*, *Hsp70*, *Hsp90*, ***Hspa1b***, hydrogen peroxide, *Ifng*, *Isg20l1*, *Lamp1*, *Lrp1*, *Mbd1*, *Nol3*, *Pka*, *Ppfibp1*, RNA pol2-transcription factor, RNA polymerase II, *Rpl21*, *Smtn*, *Sncg*, *Supt16h*, *Ube2e1*, Ubiquitin, *Ung*	Cellular development, cellular growth and proliferation, connective tissue development and function
5	*Cdh3*, *Dpyd*	Cancer, drug metabolism, genetic disorder

Biologically relevant networks extracted by IPA are shown for gene expression data after (A) DEN-4 h, (B) DEN-28 d, (C) ENU-4 h or (D) ENU-28 d treatment. Bold underlined genes show dose-dependent expression. Thin underlined genes are genes examined in the present study. *Pdgf bb* in Network-3 means *Pdgf* groups of *Pdgfa*, *Pdgfb*, *Pdgfc* and *Pdgfd*. *Hsp70* in Network-4 means *Hsp* groups of *Hspa14 hspa1a*, *Hspa1b*, *Hspa1l*, *Hspa2*, *Hspa4 hspa5*, *Hspa6*, *Hspa7*, *Hspa8*, and *Hspa9*.

was observed, and only *Btg2*, *Cdkn1a* and *Gdf15* showed a dose-dependent increase (Fig. 4A, Network-1). DEN-28 d-Network-2 included several different genes from those in DEN-4 h-Network-2 but had the same primary functions as for DEN-4 h-Network-2, and *Cyp21a1*, *Gdf15* and *Igfbp1* exhibited dose-dependency (Fig. 4A, Network-2). DEN-28 d-Network-3 consisted of the same genes and the same primary functions as for DEN-4 h-Network-3; however, no genes showed dose-dependency (Fig. 4A, Network-3). DEN-28 d-Network-4 contained a few different genes and primary functions from those of DEN-4 h-Network-4, but no genes showed a dose

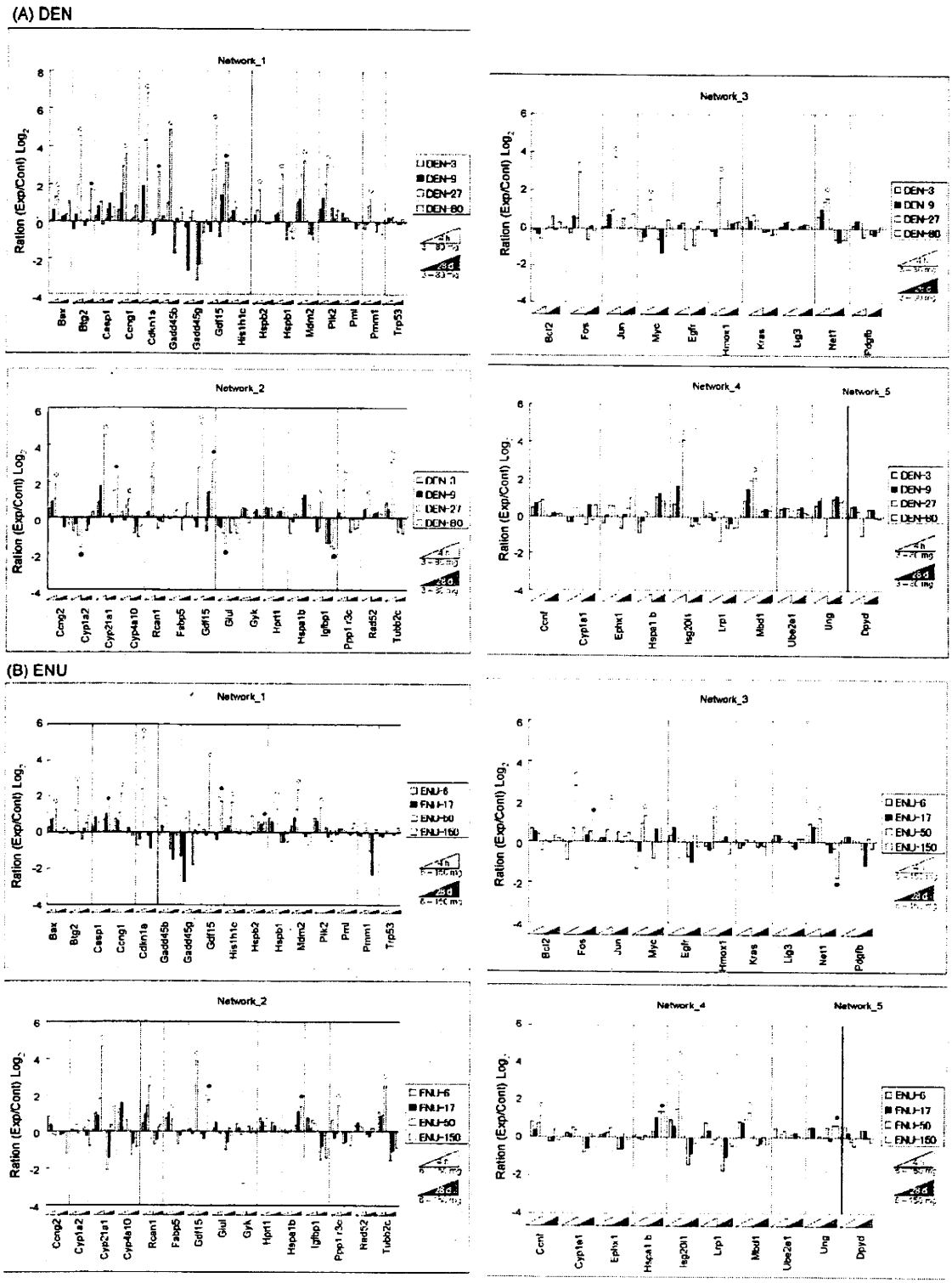

Fig. 4. Dose-dependent gene expression in each network based on different time points. The ratio values (log_2) of genes in each network are shown as bar graphs for DEN treatment (A) or ENU treatment (B). ○ shows a dose-dependent increase at 4 h, ♦ shows a dose-dependent increase at 28 days and ● shows a dose-dependent decrease.

response. DEN-28 d-Network-5 consisted of the same genes and the same top functions as those of DEN-4 h-Network-5, with no genes showing dose-dependency in this study (Fig. 4A, Network-5).

3.2. Dose-dependent alteration of gene expression induced with ENU

3.2.1. Clustering analysis for gene expression

Unsupervised hierarchical clustering results are shown in Fig. 2. The clustering presented three groups (ENU-4 h-Grp-1 to ENU-4 h-Grp-3) and two ungrouped genes for the 4 h time point after administration and four groups (ENU-28 d-Grp-1 to ENU-28 d-Grp-4) for the 28-day time point after administration. As unsupervised hierarchical clustering was performed on 4 h and 28-day data separately, group member genes were different between these two groups.

All four ENU-4 h-Grp-1 genes showed a dose-dependent increase by more than 16–32-fold 4 h after administration. Twenty-four ENU-4 h-Grp-2 genes were suggested to have a gradual dose-dependent increase of less than that of the expression in ENU-4 h-Grp-1.

All three ENU-28 d-Grp-1 genes showed a dose-dependent increase by more than two-fold 28 days after administration. Eight ENU-28 d-Grp-2 genes were suggested to have a gradual dose-dependent increase of less than that of the expression in ENU-28 d-Grp-1. *Net1* in ENU-28 d-Grp-3 showed a dose-dependent decrease of less than 0.3-fold.

Unsupervised *k*-means clustering results are shown in Fig. 3B. In the same way as for DEN, we classified these genes into four clusters based on hierarchical clustering results. For 4 h, four ENU-4 h-Cluster-1 genes exhibited a dose-dependent increase by more than 16-fold. Fourteen ENU-4 h-Cluster-2 genes exhibited a gradual dose-dependent increase as compared to genes in ENU-4 h-Cluster-1. Seven ENU-4 h-Cluster-3 genes showed an increase as a whole, with some atypical features. For 28-day data, seven ENU-28 d-Cluster-1 genes were suggested to have a tendency for a dose-dependent increase. *Net1* in ENU-28 d-Cluster-2 showed a dose-dependent decrease of less than 0.3-fold.

Two kinds of clustering results of ENU treatment are summarized as follows. A total of 29 genes showed a dose-dependent increase or decrease at 4 h or 28 days after administration. For 4 h, a total of 24 genes in ENU-4 h-Grp-1 or ENU-4 h-Grp-2 and ENU-4 h-Cluster-1, ENU-4 h-Cluster-2 or ENU-4 h-Cluster-3 showed a dose-dependent increase ranging from 2-fold to more than 32-fold [*Bax, Btg2, Ccng1, Ccnf, Cdkn1a, Cyp4a10, Cyp21a1, Fabp5, Fos, Gadd45b, Gdf15, Hist1h1c, Hmox1, Hspb1, Isg20l1, Jun, Mbd1, Mdm2, Myc, Net1, Plk2, Ppp1r3c, Rcan1* and *Tubb2c*].

For 28 days, a total of eight genes were classified as dose–response genes. Four genes in ENU-28 d-Grp-1, ENU-28 d-Grp-2, and ENU-28 d-Cluster-1 showed a dose-dependent increase of more than 2-fold [*Casp1, Fos, Gdf15* and *Hspa1b*]. Another three genes in ENU-28 d-Grp2 and ENU-28 d-Cluster-1 showed less than a two-fold increase [*Gstk1, Hspb2* and *Ung*]. *Net1* in ENU-28 d-Grp-3 and ENU-28 d-Cluster-2 showed a dose-dependent decrease of less than 0.3-fold.

3.2.2. Identification of biologically relevant networks for ENU treatment

ENU numerical data for all 51 examined genes were also analyzed by IPA for 4 h and 28-day data, and five gene networks were extracted (3). In total, the gene expression pattern for ENU was similar to the pattern for DEN; however, some differences were observed.

For 4 h, ENU-4 h-Network-1 consisted of the same genes and the same top functions as for DEN-4 h-Network-1, and 10 of these genes showed a dose-dependent increase [*Bax, Btg2, Ccng1, Cdkn1a, Gadd45b, Gdf15, Hist1h1c, Hspb1, Mdm2* and *Plk2*] (Fig. 4B, Network-1). Network-1 was the most active network for ENU-4 h. ENU-4 h-Network-2 (DNA replication, recombination, repair, cell cycle and cell signaling) included a different primary function from that of DEN-4 h-Network-2 and a few different genes from those for DEN, and seven genes showed a dose-dependent increase [*Cyp21a1, Cyp4a10, Fabp5, Gdf15, Ppp1r3c, Rcan1* and *Tubb2c*] (Fig. 4B, Network-2). ENU-4 h-Network-3 consisted of the same genes and the same top functions as those for DEN-4 h-Network-3, and five genes showed a dose-dependent increase [*Fos, Hmox1, Jun, Myc* and *Net1*] (Fig. 4B, Network-3). ENU-4 h-Network-4 also consisted of the same genes and the same top functions as those for DEN, and three genes showed a dose-dependent increase [*Ccnf, Isg20l1* and *Mbd1*] (Fig. 4B, Network-4). ENU-4 h-Network-5 consisted of the same genes and the same top functions as those for DEN-4 h-Network-5, but no genes showed a dose–response in this study (Fig. 4B, Network-5).

Network-1, Network-3 and Network-5 consisted of common genes and common top functions for both 4 h and 28 days and for both DEN and ENU. For 28 days, three genes in ENU-28 d-Network-1 showed a dose-dependent increase [*Casp1, Gdf15* and *Hspb2*] (Fig. 4B, Network-1). ENU-28 d-Network-2 included 10 different genes from those for ENU-4 h-Network-2 and had different top functions (cell signaling, molecular transport and small molecule biochemistry) from those of DEN-4 h-Network-2, DEN-28 d-Network-2 and ENU-4 h-Network-2, and 2 genes showed a dose-dependent increase [*Gdf15 and Hspa1b*] (Fig. 4B, Network-2). *Fos* and *Net1* in ENU-28 d-Network-3 showed a dose–response (Fig. 4B, Network-3). ENU-28 d-Network-4 (Table 2D) included different primary functions (cellular development, cellular growth, proliferation and connective tissue development and function) and 10 different genes from ENU-4 h-Network-4; two genes showed a dose–response [*Hspab1* and *Ung*]. ENU-28 d-Network-5 consisted of the same genes and the same top functions as those of DEN-4 h-Network-5, while no genes showed a dose–response in this study (Fig. 4A, Network-5).

4. Discussion

We examined the dose-dependency of gene expression changes for 51 genes in mouse liver treated with two *N*-nitroso genotoxic hepatocarcinogens, DEN and ENU, by qPCR at early times after administration. We selected 51 candidate genes based on our previous results of Affymetrix GeneChip Mu74AV2 and original DNA microarray of samples after treatment with DEN, dimethylnitrosamine, dipropylnitrosamine, ENU, *o*-aminoazotoluene, 7,12-dimethylbenz[*a*]anthracene, dibenzo[*a,l*]pyrene, phenobarbital and ethanol in our JEMS/MMS/Toxicogenomics group collaborative study. Because only a single dose was used for each chemical in the previous study, we examined dose-dependency in gene expression changes in this study using two representative chemicals. We showed distinct dose-dependency of gene expression changes induced by DEN and ENU; these changes associated with cancer, cell cycle arrest, DNA replication, recombination, repair and cell death not only at 4 h, but also, for some, at 28 days after administration. Similar gene expression changes between DEN and ENU were characteristic. Twenty-one genes exhibited a distinct dose-dependent increase at 4 h for both carcinogens [*Bax, Btg2, Ccng1, Cdkn1a, Cyp4a10, Cyp21a1, Fos, Gadd45b, Gdf15, Hmox1, Hspb1, Isg20l1, Jun, Mbd1, Mdm2, Myc, Net1, Plk2, Ppp1r3c, Rcan1* and *Tubb2c*], although the gene expression changed after ENU was generally weaker relative to that after DEN. The results were consistent with a previous report that showed more DNA lesions with DEN than with ENU a few hours after administration [6]. Only *Gdf15* showed a dose-dependent increase at 28 days for

both carcinogens. An additional seven different genes for DEN and eight genes for ENU also showed dose-dependency. *Ccng2*, *Hspb2*, *Igfbp1*, *Pmm1* and *Rad52* showed a dose-dependent increase and *Cyp1a2* and *Glul* showed a dose-dependent decrease 4 h after administration only with DEN. *Btg2*, *Cdkn1a* and *Cyp21a1* showed a dose-dependent increase 28 days after administration only with DEN and these genes also showed a dose–response at 4 h. *Ccnf*, *Fabp5* and *Hist1h1c* showed a dose-dependent increase 4 h after administration only with ENU. *Casp1*, *Fos*, *Gstk1*, *Hspa1b*, *Hspb2* and *Ung* showed a dose-dependent increase 28 days after administration only with ENU. *Ccnf* in DEN-4 h and *Bax* and *Ephx1* in DEN-28 d showed equivocal changes. We only observed several dose-dependent decreases in expression of genes [*Cyp1a2*, *Glul*, *Igfbp1* and *Net1*] after DEN and ENU in the present experimental conditions.

In the previous study [10], gene expression changes in number and degree were observed to peak at 4 h after administration and were lower at 20 h, 14 and 28 days. In the present study, we investigated the gene expression pattern at two different time points: 4 h, during production of many DNA lesions, and 28 days, during fixing of mutations [6]. We expected to observe the earliest and most varied effects in many cells in the liver, including DNA lesions, 4 h after administration. It was presumed that most of the DNA-damaged cells would be repaired, that some of the damaged cells would die and that only a few cells would progress to carcinogenesis. We reasoned that it would be useful to examine the earliest various effects to understand the potential gene-altering ability of carcinogens. The second time point, 28 days, is the time by which most mutations are fixed, the remainder of which would be related to carcinogenesis. We expected to observe gene expression changes which would reflect the effects of mutation at 28 days. The role of genes with altered expression might be different even if expression of the same gene was changed at 4 h and 28 days.

In addition, we examined gene networks using IPA to clarify interactions between genes with altered expression. IPA identified five networks of genes regulated at 4 h after DEN and ENU treatment (Table 3 and Fig. 4). As for DEN, 11 dose-dependent genes [*Bax*, *Btg2*, *Ccng1*, *Cdkn1a*, *Gadd45b*, *Gdf15*, *Hspb1*, *Hspb2*, *Mdm2*, *Plk2* and *Pmm1*] belonged to Network-1 (cancer and cell cycle) and the other 11 dose-dependent genes [*Ccng2*, *Cyp1a2*, *Cyp4a10*, *Cyp21a1*, *Gdf15*, *Glul*, *Igfbp1*, *Ppp1r3c Rad52*, *Rcan1* and *Tubb2c*] belonged to Network-2 (cell cycle, cell death, DNA replication, recombination and repair). In detail, *Gdf15* was extracted in both Network-1 and Network-2. As for ENU, 10 dose-dependent genes [*Bax*, *Btg2*, *Ccng1*, *Cdkn1a*, *Gadd45b*, *Gdf15*, *Hist1h1c*, *Hspb1*, *Mdm2* and *Plk2*] belonged to the same Network-1 and 7 dose-dependent genes [*Cyp21a1*, *Cyp4a10*, *Fabp5*, *Gdf15*, *Ppp1r3c*, *Rcan1* and *Tubb2c*] belonged to a different Network-2 (DNA replication, recombination and repair, and cell cycle and cell signaling). *Hspb2* and *Pmm1* showed dose–responses only in DEN-4 h-Network-1 and *Hist1h1c* showed a dose–response only in ENU-4 h-Network-1. [Cell death] in DEN-4 h-Network-2 was replaced with [Cell signaling] in ENU-4 h-Network-2. *Ccng2*, *Cyp1a2*, *Glul*, *Igfbp1* and *Rad52* showed dose–responses only in DEN-4 h-Network-2 and *Fabp5* showed a dose–response only in ENU-4 h-Network-2. This difference in Network-2 was the most remarkable difference between the effects of DEN and ENU in the present study. The top functions of Network-1 and Network-2 were characteristic networks for DEN-4 h and ENU-4 h, being typical of carcinogenic compounds. As for 28 days, IPA also identified five networks of genes, however, only a few genes showed a dose–response with DEN and ENU. As for DEN, three dose-dependent genes [*Btg2*, *Cdkn1a* and *Gdf15*] belonged to Network-1 and two genes [*Cyp21a1* and *Gdf15*] belonged to Network-2. As for ENU, three dose-dependent genes [*Casp1*, *Gdf15* and *Hspb2*] belonged to Network-1, [*Gdf15* and *Hspa1b*] belonged to Network-2, [*Fos* and *Net1*] belonged to Network-3 and [*Hspa1b* and *Ung*] belonged to Network-4. The present results suggested similar functions for *N*-nitroso carcinogens DEN and ENU, with several differences. We have examined effects of other genotoxic and non-genotoxic carcinogens in mouse liver at 4 h and have generated various networks for various carcinogens (unpublished).

We showed that Network-1 was associated with cancer and the cell cycle. To understand more detailed functions, we examined a major canonical pathway for each network. A major canonical pathway in Network-1 was *p53* signaling. The increase of *Cdkn1a*, *Ccng1* and *Gadd45* demonstrated cell cycle arrest. The expression pattern (Fig. 4) at 4 h showed that cell cycle arrest would proceed, to then be released by day 28. Both *p53* and *Bax* were associated with initiation of apoptosis.

In the same way, a major canonical pathway in Network-2 was aryl hydrocarbon receptor signaling [14]. Furthermore, aryl hydrocarbon receptor signaling as an adaptive response was manifested as the induction of xenobiotic metabolizing enzymes; *Cyp1a2*, *Cyp21a1* and *Cyp4a10* take part in this pathway. *Cyp21a1* also takes part in biosyntheses of steroid hormones [15]. Inflammation of the liver is controlled at 28 days after administration because steroid hormones function to suppress inflammation.

Growth/differentiation factor-15 (*Gdf15*) was the only gene whose expression increased at 4 h and 28 days of both DEN and ENU and belonged to Network-1 and Network-2 at 4 h and 28 days of DEN and ENU. *Gdf15* is a divergent Tgf-beta family member that is expressed following liver injury and carcinogen exposure [16]. *Gdf15* in liver is rapidly and dramatically up-regulated following various surgical and chemical treatments that cause acute liver injury and regeneration [17].

A major canonical pathway in Network-3 was platelet-derived growth factor (*Pdgf*) signaling. *Pdgfb*, *Kras*, *Jun*, *Fos* and *Myc* may be associated with *Pdgf* signaling. In this canonical pathway, *Pdgfb* phosphorylates other proteins and activates the downstream genes *Kras*, *Jun*, *Fos* and *Myc* [18–21], one reason why *Pdgfb* expression did not change significantly (Fig. 3A, Cluster-4).

Our results show that most differentially expressed genes at 4 h and 28 days exhibited a dose–response. Only a few genes, *Dpyd*, *Egfr*, *Lrp1* and *Ung* for DEN at 4 h; *Gyk* for ENU at 4 h; and *Ccng2* for ENU at 28 days showed atypical gene expression changes at the highest dose. These changes may be toxicity-related. *Dpyd* is associated with pyrimidine metabolism. *Egfr* is associated with cell proliferation. *Lrp* plays a clear protective role in atherogenesis. *Ung* is associated with DNA repair. Their decrease may show the loss of cell maintenance because hepatocytes will have received much lethal damage at the highest dose. *Gyk* is associated with xenobiotic metabolism signaling. It has been reported that glycerol kinase deficiency is involved in lipid metabolism, carbohydrate metabolism, and insulin signaling [22]. Indeed, it has been reported that type 2 diabetes is caused by ENU but not by DEN [23]. Unlike classical cyclins that promote cell cycle progression, cyclin G2 blocks cell cycle entry. The decrease of *Ccng2* mRNA may promote cell cycle progression.

Previously, we reported differential gene expression induced by two *N*-nitroso genotoxic hepatocarcinogens, DEN and dipropylnitrosamine (DPN) as compared to phenobarbital and ethanol in mouse liver examined with an original oligonucleotide microarray and qPCR [10]. We observed 11 differentially expressed genes 4 h after administration, including 7 tumor suppressor *Trp53* target genes, *Bax*, *Ccng1*, *Cdkn1a*, *Hspb2*/*Hsp27*, *Jun*, *Mdm2*, and *Plk2*/*Snk*; the other genes were *Ccnf*, *Hmox1*, *Mbd1*, and *Rad52*. Furthermore, some degree of differential gene expression of *Ccng1*, *Cdkn1a* and *Plk2*/*Snk* was observed 28 days after administration. In the present study, we selected 51 candidate genes (Table 1) based on our original DNA microarray and Affymetrix GeneChip Mu74AV2 data (not published) on seven genotoxic carcinogens, phenobarbital and ethanol. The present results show that 28 genes for

DEN and 29 genes for ENU exhibited dose-dependent differential expression. Differential gene expression was observed commonly at least for *Bax*, *Ccng1*, *Cdkn1a*, *Hmox1*, *Jun*, *Mbd1*, *Mdm2* and *Plk2* with these three *N*-nitroso carcinogens (DEN, DPN and ENU). As we expanded qPCR analysis from 14 genes in the previous study [10] to 51 genes in the present study, we could show complex gene networks by IPA. Twenty genes, *Btg2*, *Casp1*, *Ccng2*, *Cyp4a10*, *Cyp21a1*, *Ephx1*, *Gadd45b*, *Gdf15*, *Glul*, *Gstk1*, *Hspa1b*, *Hspb1*, *Igfbp1*, *Isg20l1*, *Net1*, *Pmm1*, *Ppp1r3c*, *Rcan1*, *Tubb2c* and *Ung*, which showed dose–responses in the present study, were newly examined.

We examined only pooled materials from five mice in the present study. However, we already reported that at least five genes (*Gapdh*, *Jun*, *Ccng1*, *Hspb2/Hsp27* and *Rad52*) exhibited only small inter-individual mouse gene expression variation [10] with DEN treatment after 4 h and 28 days. Additional study showed that *Bax*, *Hmox1*, *Mbd1*, *Mdm2* and *Plk2* also exhibited only small inter-individual gene expression variation with DEN treatment at 4 h and 28 days (unpublished data).

We will continue further studies on other types of chemicals for characterizing mutagenic and carcinogenic compounds; these data will be useful for chemical risk assessment and for furthering our understanding of the underlying biological processes.

Conflict of interest

We have not any conflicting interest include employment, consultancies, stock ownership, honoraria, paid expert testimony, patent applications/registrations, and grants or other funding.

Acknowledgements

This work was partly supported by KAKENHI (18310047) (C. Furihata, T. Watanabe and T. Suzuki), The Ministry of Education, Culture, Sports, Science and Technology, Japan and a High-Tech Research Center project for private universities with a matching fund subsidy from The Ministry of Education, Culture, Sports, Science and Technology, Japan (C. Furihata).

References

[1] B.A. Diwan, H. Meier, Carcinogenic effects of a single dose of diethylnitrosamine in three unrelated strains of mice: genetic dependence of the induced tumor types and incidence, Cancer Lett. 1 (1976) 249–253.
[2] A.P. Kyriazis, S.D. Vesselinovitch, Transplantability and biological behavior of mouse liver tumors induced by ethylnitrosourea, Cancer Res. 33 (1973) 332–338.
[3] J.A. Swenberg, M.C. Dyroff, M.A. Bedell, J.A. Popp, N. Huh, U. Kirstein, M.F. Rajewsky, O4-ethyldeoxythymidine, but not O6-ethyldeoxyguanosine, accumulates in hepatocyte DNA of rats exposed continuously to diethylnitrosamine, Proc. Natl. Acad. Sci. U.S.A. 81 (1984) 1692–1695.
[4] J.L. Yang, P.C. Lee, S.R. Lin, J.G. Lin, Comparison of mutation spectra induced by N-ethyl-N-nitrosourea in the hprt gene of Mer+ and Mer− diploid human fibroblasts, Carcinogenesis 15 (1994) 939–945.
[5] T. Suzuki, M. Hayashi, T. Sofuni, Initial experiences and future directions for transgenic mouse mutation assays, Mutat. Res. 307 (1994) 489–494.
[6] E.J. Mientjes, A. Luiten-Schuite, E. van der Wolf, Y. Borsboom, A. Bergmans, F. Berends, P.H. Lohman, R.A. Baan, J.H. van Delft, DNA adducts, mutant frequencies, and mutation spectra in various organs of lambda lacZ mice exposed to ethylating agents, Environ. Mol. Mutagen. 31 (1998) 18–31.
[7] J.F. Waring, R.A. Jolly, R. Ciurlionis, P.Y. Lum, J.T. Praestgaard, D.C. Morfitt, B. Buratto, C. Roberts, E. Schadt, R.G. Ulrich, Clustering of hepatotoxins based on mechanism of toxicity using gene expression profiles, Toxicol. Appl. Pharmacol. 175 (2001) 28–42.
[8] M.J. Bartosiewicz, D. Jenkins, S. Penn, J. Emery, A. Buckpitt, Unique gene expression patterns in liver and kidney associated with exposure to chemical toxicants, J. Pharmacol. Exp. Ther. 297 (2001) 895–905.
[9] M. Provenzano, S. Mocellin, Complementary techniques: validation of gene expression data by quantitative real time PCR, Adv. Exp. Med. Biol. 593 (2007) 66–73.
[10] T. Watanabe, K. Tobe, Y. Nakachi, Y. Kondoh, M. Nakajima, S. Hamada, C. Namiki, T. Suzuki, S. Maeda, A. Tadakuma, M. Sakurai, Y. Arai, A. Hyogo, M. Hoshino, T. Tashiro, H. Ito, H. Inazumi, Y. Sakaki, H. Tashiro, C. Furihata, Differential gene expression induced by two genotoxic *N*-nitroso carcinogens, phenobarbital and ethanol in mouse liver examined with oligonucleotide microarray and quantitative real-time PCR, Gene Environ. 29 (2007) 115–127.
[11] K. Sekihashi, A. Yamamoto, Y. Matsumura, S. Ueno, M. Watanabe-Akanuma, F. Kassie, S. Knasmüller, S. Tsuda, Y.F. Sasaki, Comparative investigation of multiple organs of mice and rats in the comet assay, Mutat. Res. 517 (2002) 53–75.
[12] S. Madle, S.W. Dean, U. Andrae, G. Brambilla, B. Burlinson, D.J. Doolittle, C. Furihata, T. Hertner, C.A. McQueen, H. Mori, Recommendations for the performance of UDS tests in vitro and in vivo, Mutat. Res. 312 (1994) 263–285.
[13] A. Sturn, J. Quackenbush, Z. Trajanoski, Genesis: Cluster analysis of microarray data, Bioinformatics 18 (2002) 207–208.
[14] D.W. Kim, L. Gazourian, S.A. Quadri, R. Romieu-Mourez, D.H. Sherr, G.E. Sonenshein, The RelA NF-kappaB subunit and the aryl hydrocarbon receptor (AhR) cooperate to transactivate the Myc promoter in mammary cells, Oncogene 19 (2000) 5498–5506.
[15] J. Gonçalves, A. Friães, L. Moura, Congenital adrenal hyperplasia: focus on the molecular basis of 21-hydroxylase deficiency, Expert Rev. Mol. Med. 9 (2007) 1–23.
[16] T.A. Zimmers, X. Jin, J.C. Gutierrez, C. Acosta, I.H. McKillop, R.H. Pierce, L.G. Koniaris, Effect of in vivo loss of GDF-15 on hepatocellular carcinogenesis, J. Cancer Res. Clin. Oncol. 134 (2008) 753–759.
[17] E.C. Hsiao, L.G. Koniaris, T. Zimmers-Koniaris, S.M. Sebald, T.V. Huynh, S.J. Lee, Characterization of growth-differentiation factor 15, a transforming growth factor beta superfamily member induced following liver injury, Mol. Cell. Biol. 20 (2000) 3742–3751.
[18] S. Svegliati, R. Cancello, P. Sambo, M. Luchetti, P. Paroncini, G. Orlandini, G. Discepoli, R. Paterno, M. Santillo, C. Cuozzo, S. Cassano, E.V. Avvedimento, A. Gabrielli, Platelet-derived growth factor and reactive oxygen species (ROS) regulate Ras protein levels in primary human fibroblasts via ERK1/2. Amplification of ROS and Ras in systemic sclerosis fibroblasts, J. Biol. Chem. 280 (2005) 36474–36482.
[19] J.W. Tullai, M.E. Schaffer, S. Mullenbrock, S. Kasif, G.M. Cooper, Identification of transcription factor binding sites upstream of human genes regulated by the phosphatidylinositol 3-kinase and MEK/ERK signaling pathways, J. Biol. Chem. 279 (2004) 20167–20177.
[20] A.J. Kudla, M.L. John, D.F. Bowen-Pope, B. Rainish, B.B. Olwin, A requirement for fibroblast growth factor in regulation of skeletal muscle growth and differentiation cannot be replaced by activation of platelet-derived growth factor signaling pathways, Mol. Cell. Biol. 15 (1995) 3238–3246.
[21] P.A. Bromann, H. Korkaya, C.P. Webb, J. Miller, T.L. Calvin, S.A. Courtneidge, Platelet-derived growth factor stimulates Src-dependent mRNA stabilization of specific early genes in fibroblasts, J. Biol. Chem. 280 (2005) 10253–10263.
[22] L. Rahib, N.K. MacLennan, S. Horvath, J.C. Liao, K.M. Dipple, Glycerol kinase deficiency alters expression of genes involved in lipid metabolism, carbohydrate metabolism, and insulin signaling, Eur. J. Hum. Genet. 15 (2007) 646–657.
[23] A.A. Toye, L. Moir, A. Hugill, L. Bentley, J. Quarterman, V. Mijat, T. Hough, M. Goldsworthy, A. Haynes, A.J. Hunter, M. Browne, N. Spurr, R.D. Cox, A new mouse model of type 2 diabetes, produced by N-ethyl-nitrosourea mutagenesis, is the result of a missense mutation in the glucokinase gene, Diabetes 53 (2004) 1577–1583.

Selective and direct inhibition of TRPC3 channels underlies biological activities of a pyrazole compound

Shigeki Kiyonaka[a], Kenta Kato[a], Motohiro Nishida[b], Kazuhiro Mio[c], Takuro Numaga[a], Yuichi Sawaguchi[a], Takashi Yoshida[a], Minoru Wakamori[a], Emiko Mori[a], Tomohiro Numata[a], Masakazu Ishii[d], Hiroki Takemoto[e], Akio Ojida[e], Kenta Watanabe[b], Aya Uemura[b], Hitoshi Kurose[b], Takashi Morii[f], Tsutomu Kobayashi[g], Yoji Sato[h], Chikara Sato[c], Itaru Hamachi[e], and Yasuo Mori[a,1]

[a]Laboratory of Molecular Biology, [e]Laboratory of Bioorganic Chemistry, Department of Synthetic Chemistry and Biological Chemistry, Graduate School of Engineering, Kyoto University, Kyoto 615-8510, Japan; [b]Department of Pharmacology and Toxicology, Graduate School of Pharmaceutical Sciences, Kyushu University, Higashiku, Fukuoka 812-8582, Japan; [c]Neuroscience Research Institute, National Institute of Advanced Industrial Science and Technology, Umezono 1-1-4, Tsukuba Ibaraki 305-8568, Japan; [d]Department of Pathophysiology, School of Pharmaceutical Sciences, Showa University, Tokyo 142-8555, Japan; [f]Institute of Advanced Energy, Kyoto University, Uji, Kyoto 611-0011, Japan; [g]Pharmacology Laboratory, Mitsubishi Tanabe Pharma Corporation 2-2-50, Kawagishi, Toda 335-8505, Japan; and [h]National Institute of Health Sciences, Setagaya, Tokyo 158-8501, Japan

Edited by Lutz Birnbaumer, National Institute of Environmental Health Sciences, Research Triangle Park, NC, and approved February 12, 2009 (received for review September 8, 2008)

Canonical transient receptor potential (TRPC) channels control influxes of Ca^{2+} and other cations that induce diverse cellular processes upon stimulation of plasma membrane receptors coupled to phospholipase C (PLC). Invention of subtype-specific inhibitors for TRPCs is crucial for distinction of respective TRPC channels that play particular physiological roles in native systems. Here, we identify a pyrazole compound (Pyr3), which selectively inhibits TRPC3 channels. Structure-function relationship studies of pyrazole compounds showed that the trichloroacrylic amide group is important for the TRPC3 selectivity of Pyr3. Electrophysiological and photoaffinity labeling experiments reveal a direct action of Pyr3 on the TRPC3 protein. In DT40 B lymphocytes, Pyr3 potently eliminated the Ca^{2+} influx-dependent PLC translocation to the plasma membrane and late oscillatory phase of B cell receptor-induced Ca^{2+} response. Moreover, Pyr3 attenuated activation of nuclear factor of activated T cells, a Ca^{2+}-dependent transcription factor, and hypertrophic growth in rat neonatal cardiomyocytes, and in vivo pressure overload-induced cardiac hypertrophy in mice. These findings on important roles of native TRPC3 channels are strikingly consistent with previous genetic studies. Thus, the TRPC3-selective inhibitor Pyr3 is a powerful tool to study in vivo function of TRPC3, suggesting a pharmaceutical potential of Pyr3 in treatments of TRPC3-related diseases such as cardiac hypertrophy.

Ca^{2-} signaling | pyrazole compounds | TRPC channels | TRPC3

Ca^{2+} signals control diverse cellular processes, ranging from ubiquitous activities like gene expression to tissue specific responses such as lymphocyte activation and cardiac diseases (1, 2). Stimulation of plasma membrane (PM) receptors that generates 1,4,5-trisphosphate (IP_3) and diacylglycerol (DAG) from phosphatidylinositol-4,5-bisphosphate (PIP_2) via phospholipase C (PLC) elevates cytosolic Ca^{2-} concentration ($[Ca^{2-}]_i$), which is controlled by 2 components, IP_3-induced Ca^{2+} release from intracellular Ca^{2-} store, endoplasmic reticulum (ER), and Ca^{2-} influx across PM. Ca^{2+} influx is mediated by diverse Ca^{2-}-peameable ion channels activated by various triggers (1, 2). *Drosophila transient receptor potential* (*trp*) protein and its homologues are assembled to form cation- and Ca^{2-}-permeable channels (3). Members of the "canonical" TRPC subfamily are characterized by activation induced upon stimulation of PLC-coupled receptors (4, 5). TRPC channels have been originally proposed as store-operated channels (SOC) activated by Ca^{2-} depletion of stores, whereas closely related TRPC3, TRPC6, and TRPC7 showed activation sensitivity to the membrane-delimited action of DAG (6, 7). Hence, the exact roles of TRPCs in mediating Ca^{2-} entry in response to Ca^{2+} store depletion and messenger molecules upon receptor activation remain controversial. In native systems, genetic disruption experiments have revealed important roles of TRPC1 and TRPC4 in the formation of SOCs in different cell types (8–10), and TRPC6 in receptor-operated cationic channels in vascular smooth muscle cells (11). Specific pharmacological inhibitors greatly facilitate functional identification of native TRP channel subtypes.

TRPC channels have been implicated in diverse biological functions. In B lymphocytes, TRPC1 or TRPC3 regulates B cell receptor (BCR)-mediated Ca^{2-} oscillations that activate nuclear factor of activated T cells (NFAT), a Ca^{2-}-responsive transcription factor (8). In particular, TRPC3 is associated with PLCγ2 to control amplification of receptor-mediated signals (12, 13). TRPC3 is also important in the T cell receptor-dependent Ca^{2+} entry pathway (14). Recently, studies employing transgenic mice and RNAi-mediated knockdown or overexpression strategy in cardiac myocytes have showed that TRPC3 and TRPC6 promote cardiac hypertrophy through activation of calcineurin and its downstream effector, NFAT (15–19). These results suggest TRPC channels as new targets for the development of pharmaceutical agents to treat cardiac hypertrophy. Roles are demonstrated as well for TRPC3 in the brain (20) and skeletal muscle (21), for TRPC6 in smooth muscle (22) and kidney (23), and for TRPC4 in endothelial cells (10).

Bis(trifluoromethyl)pyrazoles (BTPs) are a class of pyrazole derivatives that act as potent immunosuppressive compounds by inhibiting cytokine release from human lymphocytes and suppressing T cell proliferation (24). The BTP derivative 4-methyl-4′-[3,5-bis(trifluoromethyl)-1H-pyrazol-1-yl]-1,2,3-thiadiazole-5-carboxanilide, BTP2 (YM-58483), was shown to block SOCs in T lymphocytes and TRPC channels in HEK293 cells (25–27). Importantly, unlike other TRP inhibitors, SK&F 96365 and 2-aminoethyldiphenylborate, BTP2 is selective to TRP channels and does not affect Ca^{2+} handling by mitochondria or ER, or K^{-} channels or voltage-dependent Ca^{2+} channels (25–27). Pharmacological profiles of BTP2 have been investigated in vitro and in vivo to evaluate its potential as a therapeutic anti-asthma drug (28). However, BTP2 failed to show subtype selectivity among members of the TRPC family, inhibiting both TRPC3 and TRPC5 (27).

Author contributions: S.K., M.N., and Y.M. designed research; S.K., K.K., M.N., K.M., T. Numaga, Y. Sawaguchi, T.Y., M.W., E.M., T. Numata, M.I., H.T., K.W., and A.U. performed research; S.K., K.K., M.N., A.O., H.K., T.M., T.K., Y. Sato, C.S., I.H., and Y.M. analyzed data; and S.K., K.K., M.N., and Y.M. wrote the paper.

The authors declare no conflict of interest.

This article is a PNAS Direct Submission.

[1]To whom correspondence should be addressed. E-mail: mori@sbchem.kyoto-u.ac.jp.

This article contains supporting information online at www.pnas.org/cgi/content/full/0808793106/DCSupplemental.

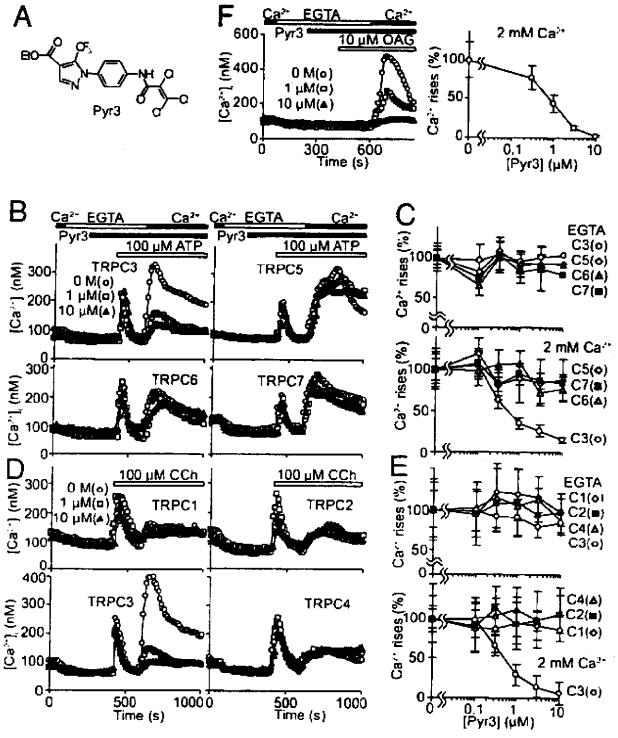

Fig. 1. Selective inhibition of TRPC3-mediated Ca^{2+} influx by Pyr3. (*A*) Chemical structure of Pyr3. (*B–E*) Concentration-dependent inhibitory action of Pyr3 on ATP receptor-induced (*B* and *C*) or mAChR-induced (*D* and *E*) induced Ca^{2+} influx via TRPCs. (*B* and *D*) Average time courses of Ca^{2+} responses induced by 100 μM ATP in HEK293 cells (*B*) or by 100 μM CCh in HEK293T cells (*D*) transfected with TRPCs at indicated Pyr3 concentrations. (*C* and *E*) Percentage peak $[Ca^{2+}]_i$ rises in Ca^{2+}-free, 0.5 mM EGTA-containing (*Upper*) or 2 mM Ca^{2+}-containing (*Lower*) external solution compared with control responses without Pyr3 (n = 33–104). (*F*) Pyr3 Inhibition of Ca^{2+} influx via OAG-activated TRPC3. Average time courses of Ca^{2+} responses induced by 10 μM OAG at indicated Pyr3 concentrations in TRPC3-transfected HEK293 cells (*Left*). Percentage peak $[Ca^{2+}]_i$ rises in 2 mM Ca^{2+} solution (*Right*) (n = 19–37).

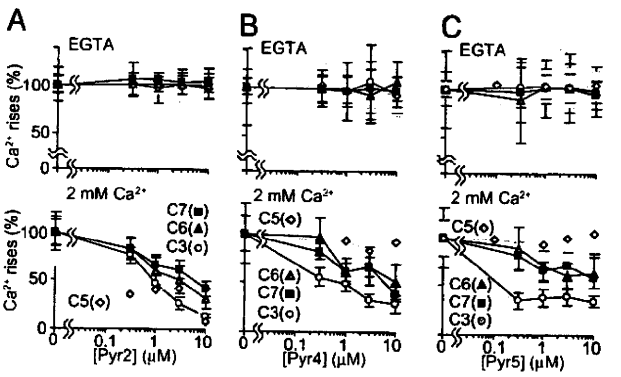

Fig. 2. Inhibition of TRPCs by Pyr2, Pyr4, or Pyr5. (*A–C*) Concentration-dependent inhibitory action of Pyr2 (*A*), Pyr4 (*B*), or Pyr5 (*C*) on Ca^{2+} influx induced by 100 μM ATP via TRPCs. Percentage peak $[Ca^{2+}]_i$ rises in Ca^{2+}-free, 0.5 mM EGTA- (*Upper*) or 2 mM Ca^{2+}-containing (*Lower*) external solution compared with control responses without drugs (n = 18–66).

Here, we study pharmacological properties of the pyrazole compound Pyr3 and demonstrate that Pyr3 selectively and directly inhibits TRPC3 channels among TRPC family members. Pyr3 potently inhibits BCR-induced responses and hypertrophic responses, in which importance of TRPC3 have been reported. Our findings suggest that Pyr3 is a useful tool for clarification of crucial and widespread functions of TRPC3 and for treatments of TRPC3-mediated diseases as well.

Results

Pyr3 Selectively Inhibits TRPC3-Mediated Ca^{2+} Influx in HEK293 Cells. Ethyl-1-(4-(2,3,3-trichloroacrylamide)phenyl)-5-(trifluoromethyl)-1H-pyrazole-4-carboxylate was synthesized as reported in ref. 24 (Fig. 1*A* and Fig. S1 in *SI Appendix*). It lacks the BTP group in contrast to BTP1 and BTP2. Therefore, we recategorized the compound together with BTP1 and BTP2 as pyrazole compounds (Pyrs), and abbreviated it as Pyr3 and BTP1 and BTP2 as Pyr1 and Pyr2, respectively. Effects of Pyr3 were examined on TRPC channel-mediated Ca^{2+} influx observed separately from Ca^{2+} release as prominent $[Ca^{2+}]_i$ rises upon readministration of Ca^{2+} to the extracellular solution under stimulation of native P2Y purinoceptors by ATP or UTP in HEK293 cells or muscarinic acetylcholine receptors (mAChR) by carbachol (CCh) in HEK293T cells (Fig. S2 in *SI Appendix*), which have only low endogenous Ca^{2+} influx activity (29). Application of Pyr3 inhibited TRPC3-mediated Ca^{2+} influx in a dose-dependent manner with the IC_{50} value of 0.7 μM (Fig. 1 *B–E* and Figs. S3 and S4 in *SI Appendix*): inhibitory action of Pyr3 became apparent at 0.3 μM, and was almost complete at 3 μM. Ten μM Pyr3 failed to significantly alter Ca^{2+} influx mediated by other TRPC members, Ca^{2+} responses in the absence of extracellular Ca^{2+} (Fig. 1 *B–E*), and the control basal $[Ca^{2+}]_i$ levels (data not shown). Interestingly, Ca^{2+} influx was inhibited by Pyr3 in cells coexpressing TRPC3 plus TRPC6 but not in cells coexpressing TRPC1 plus TRPC5 (Fig. S5 in *SI Appendix*). The results suggest a selectivity of Pyr3 to TRPC3 channels among TRPC family members and intactness of Ca^{2+} release and Ca^{2+} extrusion machinery after Pyr3 administration.

Because DAG has been suggested as a physiological activation trigger for TRPC3, TRPC6, and TRPC7 channels (6), we examined effects of Pyr3 on Ca^{2+} influx induced by the membrane-permeable DAG analogue, 1-oleoyl-2-acetyl-*sn*-glycerol (OAG) in TRPC3-transfected HEK293 cells (Fig. 1*F*). The OAG-induced Ca^{2+} influx via TRPC3 was inhibited by Pyr3 in a dose-dependent manner as observed for receptor-activated Ca^{2+} influx via TRPC3: IC_{50} of Pyr3 was 0.8 μM. The results support the TRPC3 channel as the main action site of Pyr3.

Structural Motif Important for TRPC3 Channel Selectivity on Pyr3. Pyr2 inhibited only TRPC5 at 0.3 μM. However, at higher concentrations, Pyr2 inhibited TRPC3, TRPC5, TRPC6, and TRPC7 (Fig. 2*A* and Fig. S6 *A* and *D* in *SI Appendix*) as reported in ref. 27. Thus, Pyr2 is different from Pyr3 in not distinguishing members of the TRPC family. We designed chimeric pyrazole derivatives, Pyr4 and Pyr5 (Fig. S1 in *SI Appendix*) to determine structural requirements for the selectivity to TRPC3 in Pyr3. Pyr4, a Pyr3 analogue with 4-methyl-1,2,3-thiadiazole-5-carboxyamide group of Pyr2 substituted for trichloroacrylic amide group, at 10 μM inhibited TRPC3, TRPC6, and TRPC7 but not TRPC5 (Fig. 2*B* and Fig. S6 *B* and *E* in *SI Appendix*). These results indicate a selectivity of Pyr4 to DAG-activated TRPC channels, suggesting that 3,5-bis(trifluoromethyl)pyrazole group is important for Pyr2 to recognize TRPC5. Pyr5, a Pyr3 analogue with 3,5-bis(trifluoromethyl)pyrazole group of Pyr2 substituted for ethyl-3-trifluoromethylpyrazole-4-carboxylate group, at 0.3 μM inhibited only TRPC3, suggesting that the trichloroacrylic amide group shared by Pyr3 and Pyr5 is critical for the TRPC3 selectivity (Fig. 2*C* and Fig. S6 *C* and *F* in *SI Appendix*). Interestingly, at higher concentrations such as 10 μM, Pyr5 enhanced Ca^{2+} response in vector-transfected cells or

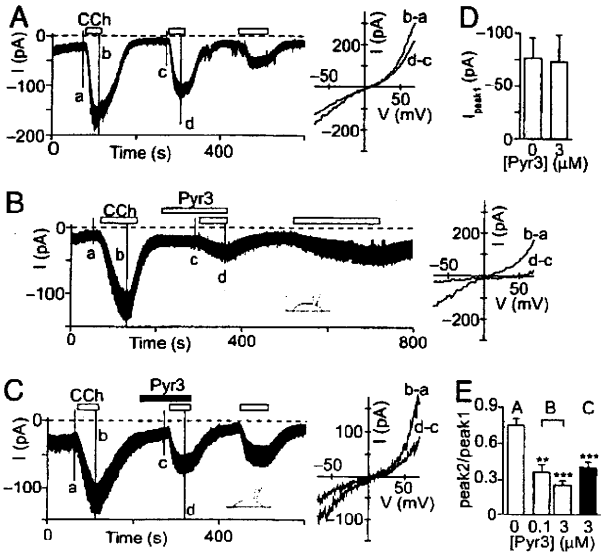

Fig. 3. mAChR-activated TRPC3 current is suppressed by extracellular application of Pyr3. (*A–C*) Traces of ionic currents induced by 60 μM CCh at a holding potential of −50 mV in TRPC3-transfected HEK293 cells (*Left*). I–V relationships obtained by subtracting the currents evoked by the voltage-ramps before activation of channels (a and c) from those after activation (current traces b and d) (*Right*). (*B*) Three μM Pyr3 is added 1.5 min before second stimulation of CCh into the external solution. (*C*) Three μM Pyr3 is added in internal solution before the recordings, and then external Pyr3 is also applied 1.5 min before second CCh stimulation. (*D*) Average current amplitudes of the first response at −50 mV in the presence (n = 7) or absence (n = 8) of 3 μM Pyr3 in the internal solution. (*E*) Concentration-dependent inhibitory action of Pyr3, using the testing paradigm depicted in *B* and *C*. The amplitude of the second response was normalized to that of the first (peak2/peak1) (n = 4–8). **, $P < 0.01$ and ***, $P < 0.001$ vs. 0 μM Pyr3.

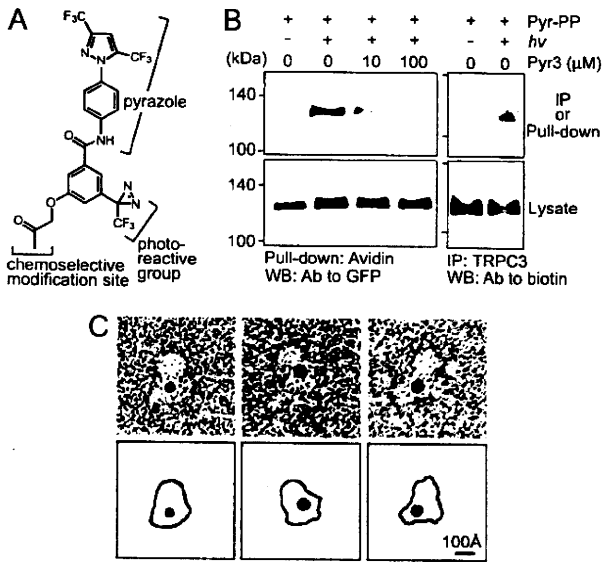

Fig. 4. Photochemical cross-linking of TRPC3 with Pyr-PP. (*A*) Chemical structure of Pyr-PP. (*B*) Pyr-PP directly binds TRPC3. After P-PALM, TRPC3-GFP proteins are detected with anti-GFP antibody by Western blot analysis (WB) in avidin pull-down samples. The photochemical Pyr-PP cross-linking of TRPC3 is inhibited by 3-min preincubation and subsequent coincubation with Pyr3 (10 or 100 μM) (*Left*). After P-PALM, the incorporation of the Pyr-PP-ARP adduct is detected with anti-biotin antibody by WB in immunoprecipitated (IP) samples with anti-TRPC3 antibody (*Right*). (*C*) Electron microscopic visualization of negatively stained TRPC3 after P-PALM with gold nanoparticles. Streptavidin-gold conjugate is attached to labeled-TRPC3 via biotin-labeling site.

at sustained phase in TRPC-expressing cells (Fig. S6*C* in *SI Appendix*), indicating a stimulatory side effect of Pyr5 on endogenous $[Ca^{2+}]_i$ regulation mechanism in HEK293 cells.

Direct Action of Pyr3 on TRPC3 Channel. Inhibitory action of Pyr3 on the TRPC3 channel was confirmed in TRPC3-transfected HEK293 cells, using the whole-cell mode of patch-clamp method (Fig. 3). When 60 μM CCh was added to stimulate endogenously expressed mAChRs, TRPC3-transfected HEK293 cells showed inward currents accompanied with an increase in the current fluctuation in the 2 mM Ca^{2+} external solution (Fig. 3*A*). Current-voltage (I–V) relationships of the currents in TRPC3-expressing cells showed a reversal potential at + 7.2 ± 3.4 mV (n = 5) and the prominent rectification at depolarizing potentials, corresponding well with those reported for receptor-activated TRPC3 currents (30). Ionic currents with a similar I–V characteristics were absent in control HEK293 cells (data not shown). The CCh-induced TRPC3 current was suppressed by extracellular perfusion of Pyr3 in a dose-dependent manner (Fig. 3 *B* and *E*) on top of run down in TRPC3 currents (Fig. 3*A*). TRPC3 maintains the same current level after washout of Pyr3 in contrast to control currents that gradually decrease with repeated CCh stimulation, suggesting that the Pyr3 block of TRPC3 is at least in part reversible but that the recovery from the blockade is a slow process (Fig. S7*A* in *SI Appendix*). Notably, because CCh induced indistinguishable Ca^{2+} response levels at the second and the third CCh stimulation in the presence and absence of Pyr3 (Fig. S7*B* in *SI Appendix*), mAChR desensitization induced by Pyr3 should be minimal if at all during repeated stimulation. Intracellular application of Pyr3 from the patch pipette failed to elicit significant changes in current levels or I–V relationships (Fig. 3 *C* and *D*), and, importantly, in susceptibility to inhibition by Pyr3 applied extracellularly (Fig. 3 *C* and *E*). OAG-activated TRPC3 currents were also inhibited by extracellular Pyr3 (3 μM) application, which failed to affect CCh- and OAG-activated TRPC6 currents (Fig. S8 in *SI Appendix*), TRPM4 currents (Fig. S9 in *SI Appendix*), and TRPM2 and TRPM7 currents (unpublished results). Inhibition of glycosylation by tunicamycin, however, failed to affect Pyr3 sensitivity of TRPC3 Ca^{2+} influx (Fig. S10 in *SI Appendix*). These results suggest that the action site of Pyr3 is located in the external side of the TRPC3 protein.

Photoaffinity labeling method is a powerful tool to identify target proteins of biologically active molecules. Recently, bifunctional photoaffinity probes having ligand moiety and biotin-tag were used for cross-linking studies of ligand/receptor complex (31). However, the introduction of a highly polar and sterically congested biotin-anchored tag to an affinity compound often resulted in marked impairment of intrinsic biological activity in the crucial probe design step. Therefore, we have carried out postphotoaffinity labeling modification (P-PALM), using a compact bifunctional Pyr probe, Pyr-PP, which carries a small functional group for selective modification by aldehyde/keto-reactive biotin derivative ARP (chemoselective modification site) and a photoreactive group for subsequent photoaffinity labeling (Fig. 4*A* and Fig. S11*A* in *SI Appendix*) (32). Importantly, Pyr-PP retained the activity to inhibit TRPC3-mediated Ca^{2+} influx (Fig. S11*B* in *SI Appendix*). In cells expressing the green fluorescent protein (GFP)-tagged TRPC3 protein, photoirradiation followed by biotin modification elicited incorporation of Pyr-PP into an ≈130-kDa protein band, which corresponds well with the molecular mass of an adduct of TRPC3-GFP (130 kDa) (Fig. 4*B Left*). Notably, Pyr-PP incorporation was inhibited

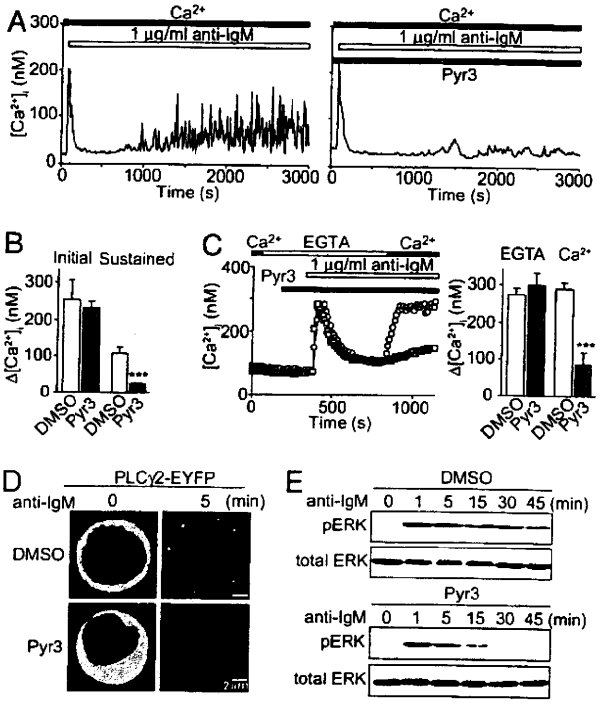

Fig. 5. Pyr3 inhibits native TRPC3 channels and downstream responses in DT40 B lymphocytes. (*A* and *B*) Inhibitory action of 0.3 μM Pyr3 on Ca^{2+} oscillation upon BCR stimulation with 1 μg/mL anti-IgM. (*A*) Representative time courses with (*Right*) or without of Pyr3 (*Left*). (*B*) Peak $[Ca^{2+}]_i$ rises at initial and sustained phases (30–40 min). (*C*) Inhibitory action of 1 μM Pyr3 on BCR-induced Ca^{2+} influx. Average time courses (*Left*). Peak $[Ca^{2+}]_i$ rises in Ca^{2+}-free, 0.5 mM EGTA- or 2 mM Ca^{2+}-containing solution (n = 42–49) (*Right*). (*D*) Confocal fluorescence images indicating PM translocation of PLCγ2-EYFP upon BCR-stimulation with 10 μg/mL anti-IgM. Three μM Pyr3 is applied 10 min before BCR stimulation. (*E*) Effects of Pyr3 on ERK activation induced by BCR stimulation (5 μg/mL anti-IgM). Three μM Pyr3 is applied 10 min before BCR stimulation. Cells are analyzed by WB, using anti-phospho-ERK2 antibody. ***, $P < 0.001$ vs. DMSO.

by coapplication of Pyr3. Furthermore, immunoprecipitation of TRPC3 followed by Western blot analysis with anti-biotin antibody strongly supports that Pyr-PP is incorporated into TRPC3 (Fig. 4*B Right*). To further confirm direct attachment of Pyr-PP on the TRPC3, biotin-labeled Pyr-PP in the negatively stained preparation was visualized with electron microscopy after incubation with streptavidin-gold conjugates (Fig. 4*C*) (33). Thus, Pyr3 selectively and directly binds to TRPC3. Interestingly, CCh failed to influence labeling of TRPC3 by Pyr-PP (Fig. S11*C* in *SI Appendix*). This is consistent with the observation that Pyr3 potently inhibited basal activity of TRPC3 but not that of TRPC6 (Fig. S12 in *SI Appendix*), excluding a possibility that receptor-induced channel activation mediates the Pyr3 action.

Pyr3 Suppresses Receptor-Activated Signaling by Inhibiting Native TRPC3 Channels in B Lymphocytes. Ca^{2+} oscillation is important for the efficiency and specificity of gene expression in lymphocytes (34). We recently reported that the Ca^{2+} oscillation is maintained by Ca^{2+} entry via TRPC3 that evokes translocation toward PM and secondary activation of PLCγ2 in DT40 B lymphocytes (13). Fig. 5*A* depicts a typical Ca^{2+} oscillation that follows initial transient Ca^{2+} responses upon stimulation of BCR in DT40 cells. Pyr3 significantly suppressed the Ca^{2+} oscillation (Fig. 5 *A* and *B*) and NFAT activity (Fig. S13 in *SI Appendix*), whereas it failed to suppress the initial Ca^{2+} responses. Pyr3 also suppressed BCR-induced Ca^{2+} influx but not Ca^{2+} release (Fig. 5*C*). In addition, observation by time-lapse confocal laser microscopy showed localization of EYFP-tagged PLCγ2 (PLCγ2-EYFP) near PM upon BCR stimulation, which was inhibited by 3 μM Pyr3 (Fig. 5*D*). Interestingly, coimmunoprecipitation of PLCγ1 and PLCγ2 with TRPC3 is unaffected by Pyr3 (Fig. S14 in *SI Appendix*), suggesting that Pyr3 acts independently of PLC-TRPC3 interaction. Thus, Pyr3 efficiently attenuates TRPC3-mediated PLCγ2 translocation and Ca^{2+} oscillation.

The activation of protein kinase C (PKC) by DAG promotes activation of extracellular signal-regulated kinase (ERK) through phosphorylation in DT40 cells (13). The PLCγ2 translocation and subsequent activation also enhance the downstream responses of DAG. In fact, the ERK phosphorylation maintained by BCR stimulation over 45 min became transient after application of 3 μM Pyr3 (Fig. 5*E*). Hence, Ca^{2+} influx via TRPC3 is required for full ERK activation in DT40 B lymphocytes.

Pyr3 Suppresses Cardiac Hypertrophy. Cardiac hypertrophy is an adaptive response of the heart to many forms of cardiac disease, including hypertension and mechanical load abnormalities (35). The importance of G protein-coupled receptors such as angiotensin II (Ang II) receptors, that activate PLC, is well established in cardiac hypertrophy (36). Recently, it has been revealed through siRNA strategy that Ca^{2+} influx through TRPC3 and TRPC6 activation is essential for Ang II-induced NFAT activation and cardiomyocyte hypertrophy (16). Pyr compounds were examined on hypertrophic responses in rat neonatal cardiomyocytes. The Ang II-induced NFAT translocation was suppressed by Pyr3, but weakly by Pyr2 in a concentration-dependent manner (IC_{50} value was 0.05 μM for Pyr3 and 2 μM for Pyr2) (Fig. S15 *A* and *B* in *SI Appendix*). Therefore, compared with Pyr2, Pyr3 is more potent in inhibiting NFAT signaling of cardiac myocytes. Pyr3 also suppressed the mechanical stretch-induced NFAT activation (Fig. S15*C* in *SI Appendix*). Notably, the Ang II-induced hypertrophic responses, such as actin reorganization, brain natriuretic peptide (BNP) expression, and protein synthesis were completely suppressed by Pyr3, but weakly by Pyr2 (Fig. S15 *D–F* in *SI Appendix*).

We further examined Pyr3 in pressure overload-induced cardiac hypertrophy in vivo. Importantly, systolic and diastolic blood pressure, heart rate, mortality, body weight, and weight for liver, lung, and heart were unaffected by chronic treatment with Pyr3 (0.1 $mg \cdot kg^{-1} \cdot day^{-1}$) in sham operated mice (Fig. S16*A* and Tables S1 and S2 in *SI Appendix*). In addition, transverse aortic constriction (TAC) operation significantly increased left ventricular end-systolic pressure (ESP) in mice treated with vehicle or Pyr3 (Tables S1 and S2 in *SI Appendix*), suggesting that pressure overload was equally induced in these mice. Strikingly, increased size of the heart by 1-week TAC operation was significantly attenuated by Pyr3 (Fig. 6 *A* and *B* and Fig. S16*B* in *SI Appendix*). The Pyr3 effect refers to concentric hypertrophy, because the ratio of internal ventricular radius at end diastole (r) to ventricular wall thickness (h) was significantly decreased in echocardiography in mid transverse heart sections (Fig. 6*A* and Fig. S16*C* in *SI Appendix*), in contrast to fractional shortening (FS) and the right ventricle unaffected by TAC (Fig. S16 *D* and *E* in *SI Appendix*). The TAC-induced increase in expression of atrial natriuretic peptide (ANP) mRNA, a reliable marker for cardiac hypertrophy, was also suppressed by Pyr3 (Fig. 6*C*). Six-weeks TAC operation induced an r/h ratio increase characteristic of dilated hypertrophy (Fig. S16*F* in *SI Appendix*), and deterioration of FS and elevation of weight-to-tibia length ratio of the left ventricle (LVW/TL) in good correlation with systolic pressure gradient. These symptoms were suppressed by Pyr3 (Fig. 6 *D* and *E*). Thus, Pyr3 is potent against concentric and dilated cardiac hypertrophy.

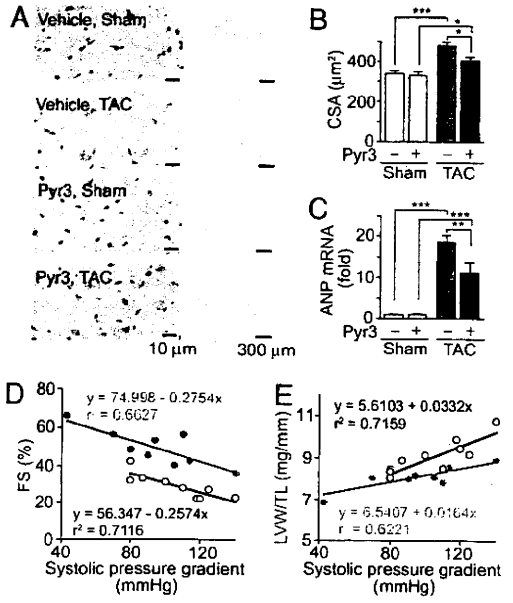

Fig. 6. Potent suppressive effects of Pyr3 on cardiac hypertrophy induced by pressure overload in mice. (*A–C*) Effects of Pyr3 on 1-week TAC-induced concentric hypertrophy. (*A*) H&E-stained mid transverse sections of hearts isolated from sham- and TAC-operated mice. (*B* and *C*) Effects of Pyr3 on the increase in cross-sectional areas (CSA) (*B*) and ANP mRNA expressions (*C*). *, $P < 0.05$, **, $P < 0.01$, and ***, $P < 0.001$. (*D* and *E*) Effects of Pyr3 on 6-weeks TAC-induced dilated hypertrophy. Scattergram of systolic pressure gradient vs. FS, a surrogate of systolic function (*D*) and LVW/TL (*E*) in TAC-operated mice with (red) and without (black) treatment with Pyr3. Pyr3 significantly shifts relationships upward in FS ($P < 0.001$) and downward in LVW/TL ($P < 0.01$).

Discussion

The present investigation demonstrates a potent inhibitory action of Pyr3 on both recombinant and native TRPC3 channels. Photoaffinity labeling with Pyr-PP reveals direct action of Pyr3 on the TRPC3 channel. Pyr3 efficiently suppressed biological responses in which critical involvements of TRPC3 have been reported. In B lymphocytes, Pyr3 eliminated the BCR-induced Ca^{2+} oscillation regulated by TRPC3-mediated Ca^{2+} influx. In the cardiac system, Pyr3 attenuates NFAT activation and hypertrophic growth in myocytes and pressure overload-induced hypertrophy in vivo.

BTPs were originally identified as inhibitors of T lymphocyte activation (24). Several reports have suggested that BTP2 (Pyr2) is a potent inhibitor for both Ca^{2+} release-activated Ca^{2+} (CRAC) channels and TRPC channels and for NFAT-driven IL-2 production (25–27). Structure-function relationships in BTPs proposed that 4′-[3,5-bis(trifluoromethyl)pyrazol-1-yl]-carboxanilide moiety is useful for discovering potent inhibitors for CRAC channels (37). However, here we demonstrate that the 3,5-bis(trifluoromethyl)pyrazole group is not required for the inhibition of TRPC3, because Pyr3 without this group selectively inhibited TRPC3 channel, and is more potent than Pyr2 in inhibiting NFAT of cardiac myocytes. Moreover, our structure-function relationship study using Pyr4 and Pyr5 demonstrates that the 3,5-bis(trifluoromethyl)pyrazole or trichloroacrylic amide group is critical for the selectivity of Pyr4 or Pyr5 to TRPC5 or TRPC3, respectively. Thus, pyrazole group provides a molecular skeleton to invent potent inhibitors for each TRPC.

It has been suggested that Pyr2 activates the Ca^{2+}-activated nonselective cation channel TRPM4 that decreases Ca^{2+} influx by depolarizing membrane potential and reducing the Ca^{2+} entry driving force in lymphocytes (38). This contradicts with the report that Pyr2 failed to alter membrane potential in Jurkat cells (25). In addition, when external Na^+ ions were completely replaced by the nonpermeant organic cation *N*-methyl-D-glucamine, Sr^{2+} influx activated by CCh still showed an intact sensitivity to Pyr2, leading to an idea that the action of Pyr2 to block TRPC3 channels is independent of the membrane-depolarizing action of TRPM4 (27). This idea is consistent with our results. Importantly, if Pyr3 activates TRPM4-mediated membrane depolarization, it should also inhibit receptor-activated Ca^{2+} influx via TRPC channels other than TRPC3. However, this is not the case. Hence, the action of Pyrs is mainly attributable to inhibition of TRPCs.

Pyr2 unlikely acts from the cytosolic side of CRAC channels, for instance, by inhibiting the activation mechanism or the intracellular part of the channel pore (26). It has been also proposed that Pyr2 inhibits TRPC3 by preventing channel interactions with DAG or by compromising the conformational change in the channels that leads to opening (27). We have confirmed direct action of Pyrs on TRPC3 through observation that Pyr3 inhibition of TRPC3 activity or incorporation of Pyr-PP does not require receptors or their activation. Electrophysiological recording (Fig. 3) locates the action site on the extracellular side of TRPC3 proteins. Amino acid residues unique for TRPC3 in functionally important domains such as E3 (39) may be responsible for the TRPC3 selectivity of Pyr3. Recently, we reported a reconstruction of a 3-dimentional (3D) structure of TRPC3 at 15 Å resolution by single particle analysis of images taken by a cryoelectron microscope (33). It would be interesting to locate Pyr-binding site in 3D reconstitution of TRPC3 proteins at this resolution.

Functions of native TRPC3 channels are yet to be established. Initial overexpression studies reported that TRPC3 forms SOCs (5). However, constitutive channel activity suppressed by strong intracellular Ca^{2+} buffering (40, 41) and DAG-induced activation via a membrane-delimited pathway have been reported for TRPC3 (6). Therefore, depending on the expression system and protein expression levels, TRPC3 can function in a store-dependent or -independent manner (42, 43). Physical interactions have been suggested for TRPC3 also with IP_3 receptors, PLCγ1, and PLCγ2 (12, 13, 44). Interestingly, BCR stimulation failed to induce PLCγ2 translocation to PM in DT40 B cell mutant lines engineered with disruption of TRPC3 localization at PM (unpublished results), in support of the importance of TRPC3 in the PLCγ2 translocation. We have also found that TRPC3 mediates Ca^{2+} influx responsible for translocation of PKCβ to the PM and anchors PKCβ at PM. This suggests that TRPC3 functions not only as an ion conducting channel but also as a protein scaffold. Pyr3 should be extremely useful in selectively dissecting multiple roles of native TRPC3.

$[Ca^{2+}]_i$ elevation by various hypertrophic stimuli plays a critical role in the development of cardiac hypertrophy (36). Continuous blockage of L-type voltage-dependent Ca^{2+} channels by Ca^{2+} antagonists effectively suppresses the development of cardiac hypertrophy (16). However, because L-type Ca^{2+} channels controls excitation-contraction coupling, these Ca^{2+} channel antagonists may exert serious influence on the myocardial contraction. Recently, TRPC3 and TRPC6 channels have been reported to regulate cardiac hypertrophy (15–19). Suppression of Ang II- or mechanical stretch-induced NFAT activation and hypertrophic growth of cardiomyoctes by Pyr3 strongly suggest a potential of Pyr3 in the treatment of cardiac hypertrophy. Compared with Pyr2, which was reported to inhibit ANP secretion and β-myosin heavy chain expression in rat neonatal ventricular myocytes stimulated with α-adrenergic agonist, phenylephrine (15), Pyr3 has improved potency in inhibiting hypertrophic responses. Moreover, attenuation of pressure over-

load-induced cardiac hypertrophy in vivo by Pyr3 will give efficacy for the pathological heart without serious influence of the normal myocardial contraction. This Pyr3 property may lead to a safer therapeutic approach to cardiac hypertrophy.

Methods

The detailed methods for cell culture and cDNA expression, $[Ca^{2+}]_i$ measurements, electrophysiology, photoaffinity labeling, coimmunoprecipitation, confocal image analysis, measurements of NFAT and ERK activation, and analysis of cardiac hypertrophy in vitro and in vivo are described in *SI Appendix*.

ACKNOWLEDGMENTS. We thank N. Onohara and S. Tanabe for technical support. This work was supported by grants from the Ministry of Education, Culture, Sports, Science and Technology, Core Research for Evolutional Science and Technology, and the National Institute of Biomedical Innovation of Japan.

1. Abramowitz J, Birnbaumer L (2009) Physiology and pathophysiology of canonical transient receptor potential channels. *FASEB J* 23:297–328.
2. Nilius B, Owsianik G, Voets T, Peters JA (2007) Transient receptor potential channels in disease. *Physiol Rev* 87:165–217.
3. Hardie RC, Minke B (1992) The *trp* gene is essential for a light-activated Ca^{2+} channel in Drosophila photoreceptors. *Neuron* 8:643–651.
4. Venkatachalam K, Montell C (2007) TRP channels. *Annu Rev Biochem* 76:387–417.
5. Zhu X, et al. (1996) *trp*, a novel mammalian gene family essential for agonist-activated capacitative Ca^{2+} entry. *Cell* 85:661–671.
6. Hofmann T, et al. (1999) Direct activation of human TRPC6 and TRPC3 channels by diacylglycerol. *Nature* 397:259–263.
7. Okada T, et al. (1999) Molecular and functional characterization of a novel mouse transient receptor potential protein homologue TRP7. *J Biol Chem* 274:27359–27370.
8. Mori Y, et al. (2002) Transient receptor potential 1 regulates capacitative Ca^{2+} entry and Ca^{2+} release from endoplasmic reticulum in B lymphocytes. *J Exp Med* 195:673–681.
9. Liu X, et al. (2007) Attenuation of store-operated Ca^{2+} current impairs salivary gland fluid secretion in TRPC1(−/−) mice. *Proc Natl Acad Sci USA* 104:17542–17547.
10. Freichel M, et al. (2001) Lack of an endothelial store-operated Ca^{2+} current impairs agonist-dependent vasorelaxation in $TRP4^{-/-}$ mice. *Nat Cell Biol* 3:121–127.
11. Inoue R, et al. (2001) The transient receptor potential protein homologue TRP6 is the essential component of vascular α_1-adrenoceptor-activated Ca^{2+}-permeable cation channel. *Circ Res* 88:325–332.
12. Patterson RL, et al. (2002) Phospholipase C-γ is required for agonist-induced Ca^{2+} entry. *Cell* 111:529–541.
13. Nishida M, et al. (2003) Amplification of receptor signalling by Ca^{2+} entry-mediated translocation and activation of PLCγ2 in B lymphocytes. *EMBO J* 22:4677–4688.
14. Philipp S, et al. (2003) TRPC3 mediates T-cell receptor-dependent calcium entry in human T-lymphocytes. *J Biol Chem* 278:26629–26638.
15. Bush EW, et al. (2006) Canonical transient receptor potential channels promote cardiomyocyte hypertrophy through activation of calcineurin signaling. *J Biol Chem* 281:33487–33496.
16. Onohara N, et al. (2006) TRPC3 and TRPC6 are essential for angiotensin II-induced cardiac hypertrophy. *EMBO J* 25:5305–5316.
17. Brenner JS, Dolmetsch RE (2007) TrpC3 regulates hypertrophy-associated gene expression without affecting myocyte beating or cell size. *PLoS ONE* 2:e802.
18. Nakayama H, Wilkin BJ, Bodi I, Molkentin JD (2006) Calcineurin-dependent cardiomyopathy is activated by TRPC in the adult mouse heart. *FASEB J* 20:1660–1670.
19. Kuwahara K, et al. (2006) TRPC6 fulfills a calcineurin signaling circuit during pathologic cardiac remodeling. *J Clin Invest* 116:3114–3126.
20. Li HS, Xu XZ, Montell C (1999) Activation of a TRPC3-dependent cation current through the neurotrophin BDNF. *Neuron* 24:261–273.
21. Rosenberg P, et al. (2004) TRPC3 channels confer cellular memory of recent neuromuscular activity. *Proc Natl Acad Sci USA* 101:9387–9392.
22. Dietrich A, et al. (2005) Increased vascular smooth muscle contractility in *TRPC6*$^{-/-}$ mice. *Mol Cell Biol* 25:6980–6989.
23. Winn MP, et al. (2005) A mutation in the *TRPC6* cation channel causes familial focal segmental glomerulosclerosis. *Science* 308:1801–1804.
24. Djuric SW, et al. (2000) 3,5-Bis(trifluoromethyl)pyrazoles: A novel class of NFAT transcription factor regulator. *J Med Chem* 43:2975–2981.
25. Ishikawa J, et al. (2003) A pyrazole derivative, YM-58483, potently inhibits store-operated sustained Ca^{2+} influx and IL-2 production in T lymphocytes. *J Immunol* 170:4441–4449.
26. Zitt C, et al. (2004) Potent inhibition of Ca^{2+} release-activated Ca^{2+} channels and T-lymphocyte activation by the pyrazole derivative BTP2. *J Biol Chem* 279:12427–12437.
27. He L-P, Hewavitharana T, Soboloff J, Spassova MA, Gill DL (2005) A functional link between store-operated and TRPC channels revealed by the 3,5-bis(trifluoromethyl)pyrazole derivative, BTP2. *J Biol Chem* 280:10997–11006.
28. Ohga K, et al. (2008) The suppressive effects of YM-58483/BTP-2, a store-operated Ca^{2+} entry blocker, on inflammatory mediator release in vitro and airway responses in vivo. *Pulm Pharmacol Ther* 21:360–369.
29. Okada T, et al. (1998) Molecular cloning and functional characterization of a novel receptor-activated TRP Ca^{2+} channel from mouse brain. *J Biol Chem* 273:10279–10287.
30. Trebak M, Bird GS, McKay RR, Birnbaumer L, Putney JW Jr (2003) Signaling mechanism for receptor-activated canonical transient receptor potential 3 (TRPC3) channels. *J Biol Chem* 278:16244–16252.
31. Tomohiro T, Hashimoto M, Hatanaka Y (2005) Cross-linking chemistry and biology: Development of multifunctional photoaffinity probes. *Chem Rec* 5:385–395.
32. Nagase T, Shinkai S, Hamachi I (2001) Post-photoaffinity labeling modification using aldehyde chemistry to produce a fluorescent lectin toward saccharide-biosensors. *Chem Commun* 229–230.
33. Mio K, et al. (2007) The TRPC3 channel has a large internal chamber surrounded by signal sensing antennas. *J Mol Biol* 367:373–383.
34. Tomida T, Hirose K, Takizawa A, Shibasaki F, Iino M (2003) NFAT functions as a working memory of Ca^{2+} signals in decoding Ca^{2+} oscillation. *EMBO J* 22:3825–3832.
35. Frey N, Olson EN (2003) Cardiac hypertrophy: The good, the bad, and the ugly. *Annu Rev Physiol* 65:45–79.
36. Molkentin JD, Dorn II GW (2001) Cytoplasmic signaling pathways that regulate cardiac hypertrophy. *Annu Rev Physiol* 63:391–426.
37. Yonetoku Y, et al. (2006) Novel potent and selective calcium-release-activated calcium (CRAC) channel inhibitors. Part 2: Synthesis and inhibitory activity of aryl-3-trifluoromethylpyrazoles. *Bioorg Med Chem* 14:5370–5383.
38. Takezawa R, et al. (2006) A pyrazole derivative potently inhibits lymphocyte Ca^{2+} influx and cytokine production by facilitating transient receptor potential melastatin 4 channel activity. *Mol Pharmacol* 69:1413–1420.
39. Xu SZ, et al. (2005) Generation of functional ion-channel tools by E3 targeting. *Nat Biotechnol* 23:1289–1293.
40. Zitt C, et al. (1997) Expression of TRPC3 in Chinese hamster ovary cells results in calcium-activated cation currents not related to store depletion. *J Cell Biol* 138:1333–1341.
41. Kiselyov K, Mignery GA, Zhu MX, Muallem S (1999) The N-terminal domain of the IP_3 receptor gates store-operated hTrp3 channels. *Mol Cell* 4:423–429.
42. Vazquez G, Lievremont JP, St J Bird G, Putney JW Jr (2001) Human Trp3 forms both inositol triphosphate receptor-dependent and receptor-independent store-operated cation channels in DT40 avian B lymphocytes. *Proc Natl Acad Sci USA* 98:11777–11782.
43. Trebak M, Bird GS, McKay RR, Putney JW Jr (2002) Comparison of human TRPC3 channels in receptor-activated and store-operated modes. Differential sensitivity to channel blockers suggests fundamental differences in channel composition. *J Biol Chem* 277:21617–21623.
44. Boulay G, et al. (1999) Modulation of Ca^{2+} entry by polypeptides of the inositol 1,4,5-trisphosphate receptor (IP3R) that bind transient receptor potential (TRP): Evidence for roles of TRP and IP3R in store depletion-activated Ca^{2+} entry. *Proc Natl Acad Sci USA* 96:14955–14960.

Generation of Mouse Induced Pluripotent Stem Cells Without Viral Vectors

Keisuke Okita,[1] Masato Nakagawa,[1,2] Hong Hyenjong,[2] Tomoko Ichisaka,[1,3] Shinya Yamanaka[1,2,3,4]*

Induced pluripotent stem (iPS) cells have been generated from mouse and human somatic cells by introducing Oct3/4 and Sox2 with either Klf4 and c-Myc or Nanog and Lin28 using retroviruses or lentiviruses. Patient-specific iPS cells could be useful in drug discovery and regenerative medicine. However, viral integration into the host genome increases the risk of tumorigenicity. Here, we report the generation of mouse iPS cells without viral vectors. Repeated transfection of two expression plasmids, one containing the complementary DNAs (cDNAs) of Oct3/4, Sox2, and Klf4 and the other containing the c-Myc cDNA, into mouse embryonic fibroblasts resulted in iPS cells without evidence of plasmid integration, which produced teratomas when transplanted into mice and contributed to adult chimeras. The production of virus-free iPS cells, albeit from embryonic fibroblasts, addresses a critical safety concern for potential use of iPS cells in regenerative medicine.

iPS cells were first generated from mouse fibroblasts by retroviral-mediated introduction of four factors, Oct3/4, Sox2, Klf4, and c-Myc (*1*). Human fibroblasts can also be reprogrammed by the same four factors (*2–4*) or by Oct3/4, Sox2, Nanog, and Lin28 (*5*). Mouse and human iPS cells are similar to embryonic stem (ES) cells in morphology, gene expression, epigenetic status, and in vitro differentiation. Furthermore, mouse iPS cells give rise to adult chimeras and show competence for germline transmission (*6–8*). However, chimeras and progeny mice derived from iPS cells frequently develop tumors, which in some cases may be due to reactivation of the c-Myc oncogene (*7*). It is possible to generate iPS cells without retroviral insertion of c-Myc (*9*, *10*), albeit at a lower efficiency. Nevertheless, retroviral integration of the other transcription factors may activate or inactivate host genes, resulting in tumorigenicity, as was the case in some patients who underwent gene therapy (*11*). In order to apply the technology to cell transplantation therapy, it is crucial to generate iPS cells with use of nonintegration methods (*12*).

To generate mouse iPS cells without retroviruses, we used an adenovirus-mediated gene delivery system. As an initial step, we generated iPS cells with one or two factors using adenoviruses and using retroviruses for the remaining factors. We used mice in which green fluorescence protein (GFP) and the puromycin-

[1]Center for iPS Cell Research and Application (CiRA), Institute for Integrated Cell-Material Sciences, Kyoto University, Kyoto 606-8507, Japan. [2]Department of Stem Cell Biology, Institute for Frontier Medical Sciences, Kyoto University, Kyoto 606-8507, Japan. [3]Core Research for Evolutional Science and Technology and Yamanaka iPS Cell Project, Japan Science and Technology Agency, Kawaguchi 332-0012, Japan. [4]Gladstone Institute of Cardiovascular Disease, San Francisco, CA 94158, USA.

*To whom correspondence should be addressed. E-mail: yamanaka@frontier.kyoto-u.ac.jp

resistant gene are driven by the *Nanog* enhancer and promoter (*7*). With the Nanog reporter, iPS cells can be selected with puromycin and detected as GFP-positive colonies. We transduced mouse primary hepatocytes from the Nanog reporter mice with combinations of retroviruses and adenoviruses. We chose hepatocytes because iPS cells derived from hepatocytes have fewer retroviral integration sites than do iPS cells derived from fibroblasts (*13*). Because transgene expression should be maintained for up to 12 days during iPS cell generation (*14*, *15*), we repeatedly delivered adenoviruses. We observed GFP-positive colonies when Sox2 or Klf4 was introduced with adenovirus and the remaining two factors–Oct3/4 and Klf4 or Oct3/4 and Sox2, respectively–were introduced with retroviruses (Fig. 1A). We confirmed that these iPS cells did not show integration of adenoviral transgenes (Fig. 1B). They expressed markers of ES cells, including Nanog, Rex1, and ECAT1, in quantities similar to those in ES cells (Fig. 1C). They formed teratomas containing derivatives of all three germ layers when transplanted subcutaneously into nude mice (Fig. 1D). No GFP-positive colonies emerged when Oct3/4 was introduced with adenoviruses and Klf4 and Sox2 with retroviruses (Fig. 1A). Furthermore, we did not obtain GFP-positive colonies upon introduction of two factors by adenoviruses.

We were unable to generate iPS cells by introducing the four factors with separate adenoviral vectors. This might be due to the inability to introduce multiple factors into the same cells at sufficient concentrations. Hence, we placed the cDNAs encoding Oct3/4, Sox2, and Klf4 into a single expression vector. To this end, we used the foot-and-mouth disease virus 2A self-cleaving peptide (*16*, *17*), which enables efficient polycistronic expression in ES cells. We first placed the three cDNAs in all possible orders into pMXs retroviral vectors (*18*) (fig. S1A). We then transduced Nanog reporter mouse embryonic fibroblasts (MEFs) with these retroviruses to induce iPS cells. We observed the highest efficiency of GFP-positive colony formation when the factors were in order as Oct3/4, Klf4, and then Sox2 (fig. S1, B and C).

Next, we placed the three factors in this same order into a plasmid vector containing the CAG constitutively active promoter (*19*) (pCX-OKS-2A, Fig. 2A). In addition, we constructed another plasmid to express c-Myc (pCX-cMyc, Fig. 2A). In the initial attempt (experiment number 432), we transfected pCX-OKS-2A on days 1 and 3 and pCX-cMyc on days 2 and 4 (Fig. 2B). We obtained GFP-positive colonies that were morphologically indistinguishable from mouse ES cells (Fig. 2C). These virus-free iPS cells expressed ES cell marker genes at levels comparable to those in ES cells (Fig. 2D) and gave rise to adult chimeric mice (Fig. 2E). These data showed that mouse iPS cells can be generated without retroviruses or lentiviruses. Polymerase chain reaction (PCR) analyses, however, detected plasmid incorporation into the host genome (Fig. 2F).

We then modified the transfection protocol in order to avoid plasmid integration. We transfected pCX-OKS-2A and pCX-cMyc together on days 1, 3, 5, and 7 (experiment number 440, Fig. 2B). We obtained multiple GFP-positive colonies, which gave rise to cells morphologically indistinguishable from ES cells (Fig. 2C). These cells expressed markers of ES cells at comparable levels (Fig. 2D). To test for genomic integration of plasmid DNA, we designed 16 sets of PCR

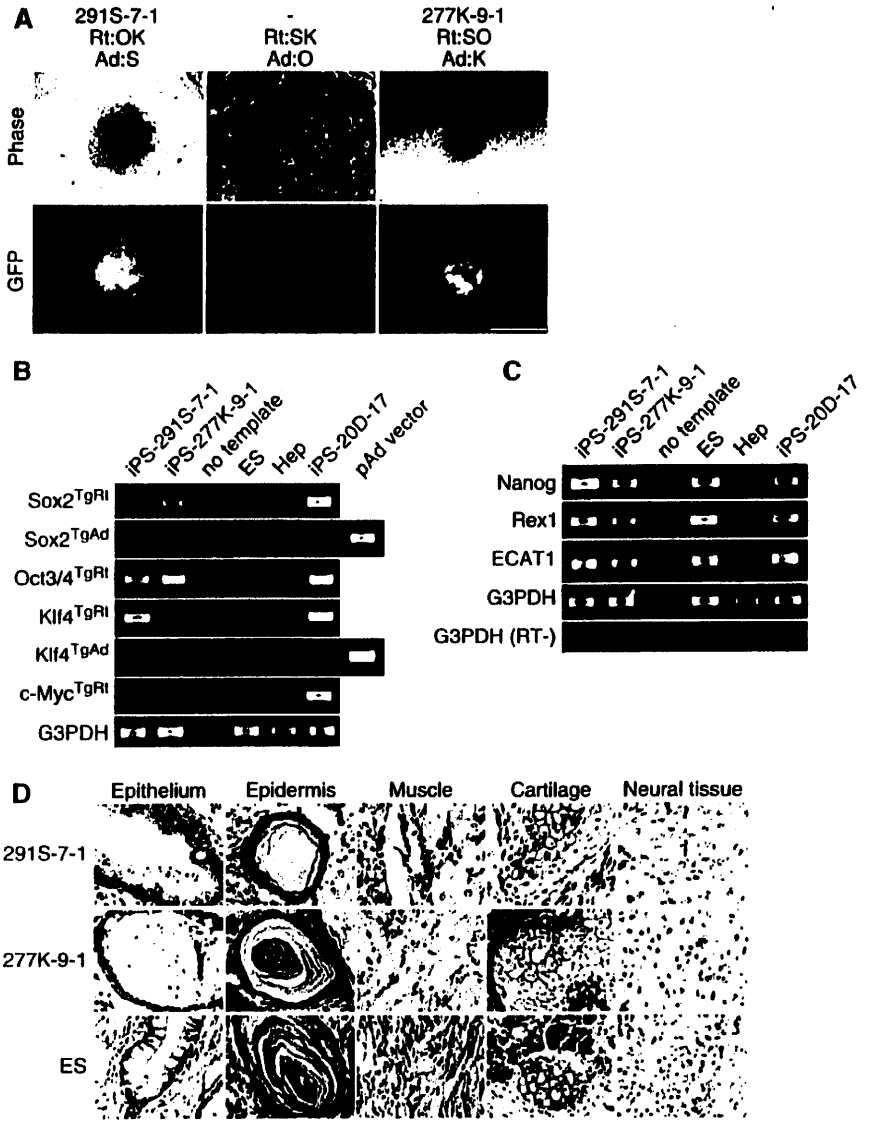

Fig. 1. Generation of iPS cells with adenovirus/retrovirus combination. **(A)** Morphology of iPS cells established by adenovirus/retrovirus combination. The iPS cell clone 291S-7-1 was generated with retroviral (Rt) introduction of Oct3/4 (O) and Klf4 (K) and adenoviral (Ad) introduction of Sox2 (S). The iPS cell clone 277K-9-1 was generated with retroviral introduction of Oct3/4 and Sox2 and adenoviral introduction of Klf4. Scale bar indicates 500 μm. **(B)** Integration of retroviral transgenes (TgRt) and adenoviral transgenes (TgAd) of the four factors was examined by genomic PCR analyses. As a control of TgRt, iPS cells generated with retroviruses (clone 20D-17) were used. As a control of TgAd, the plasmid pAd/CMV/V5-DEST vectors containing Sox2 or Klf4 were used. ES, RF8 mouse ES cells; Hep, mouse primary hepatocytes. As a loading control, the housekeeping gene, glyceraldehyde-3-phosphate dehydrogenase (G3PDH) was used. **(C)** Reverse transcription PCR (RT-PCR) analyses of ES cell marker genes and transgenes in RF8 mouse ES cells and iPS cells (clones 291S-7-1, 277K-9-1, and 20D-17). As a loading control, G3PDH was used. As a negative control, G3PDH was amplified without the reverse transcriptase (RT–). **(D)** Teratoma formation. RF8 ES cells or iPS cells (clones 291S-7-1 and 277K-9-1) were subcutaneously transplanted into nude mice. After 4 weeks, tumors were sectioned and stained with hematoxylin and eosin staining. Shown are gutlike epithelial tissues (left), epidermal tissues, striated muscles, cartilage, and neural tissues (right).

primers to amplify various parts of the plasmids (Fig. 2A). In 9 out of 11 GFP-positive clones obtained by the modified protocol, no amplification of plasmid DNA was observed (Fig. 2F). In addition, Southern blot analyses did not detect integration of transgenes in these clones (fig. S2). Although we cannot formally exclude the presence of small plasmid fragments, these data show that the iPS cells are most likely free from plasmid integration into the host genome.

To exclude the possibility that virus-free iPS cells were derived from contamination of Nanog reporter ES cells that we have in our laboratory, we performed simple sequence length polymorphisms (SSLP) analyses. In experiment number

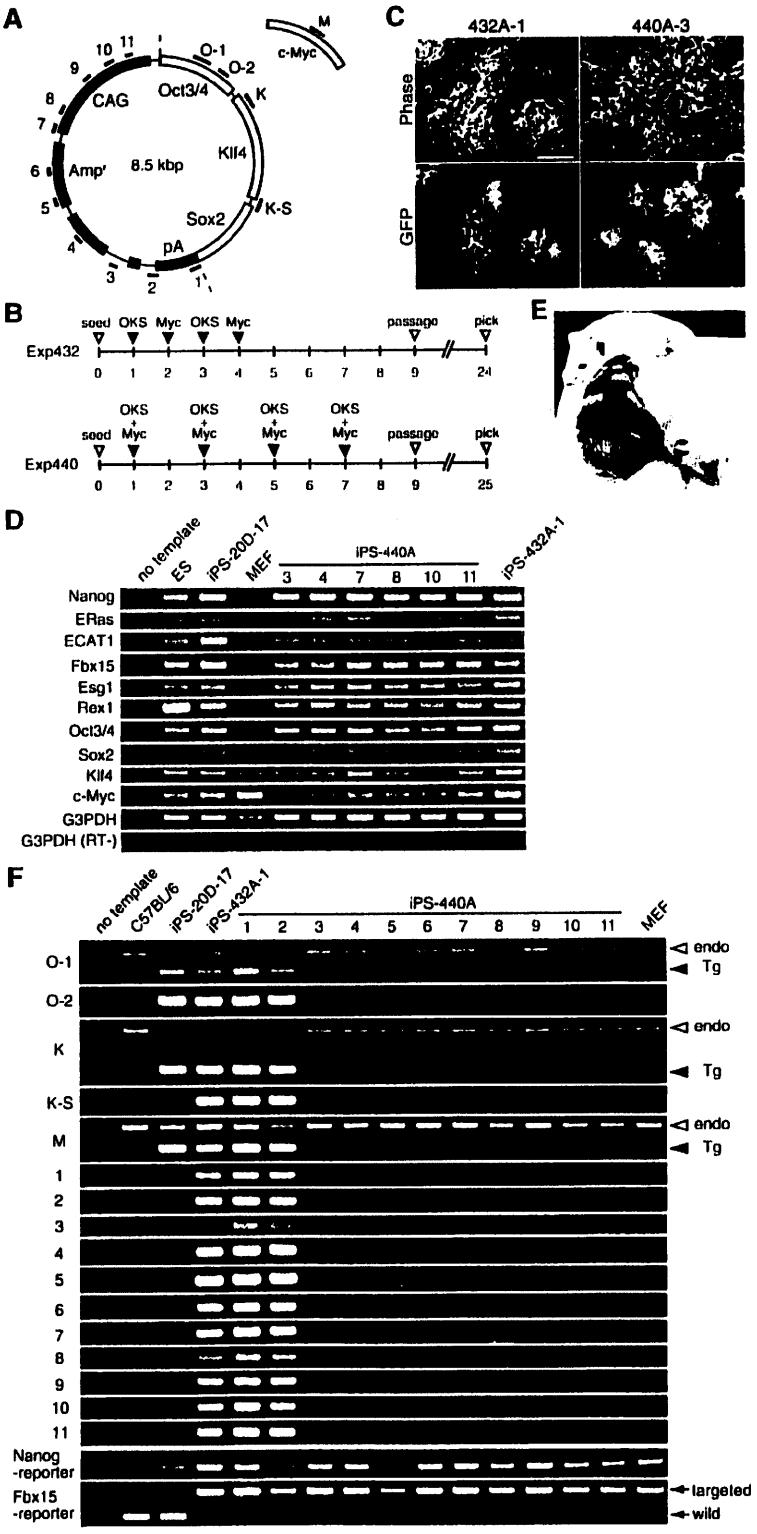

Fig. 2. Generation of virus-free iPS cells. **(A)** Expression plasmids for iPS cell generation. The three cDNAs encoding Oct3/4, Klf4, and Sox2 were connected in this order with the 2A peptide and inserted into the pCX plasmid (pCX-OKS-2A). In addition, the c-Myc cDNA was inserted into pCX (pCX-cMyc). Thick lines (O-1, O-2, K, K-S, 1 to 11, and M) indicate amplified regions used in (F) to detect plasmid integration into genome. The locations of the CAG promoter, the ampicillin-resistant gene (Amp^r), and the polyadenylation signal (pA) are also shown. **(B)** Time schedules for induction of iPS cells with plasmids. Open arrowheads indicate the timing of cell seed, passage, and colony pickup. Solid arrowheads indicate the timing of transfection. **(C)** Colonies of virus-free iPS cells. Scale bar, 200 μm. **(D)** Gene expression. Total RNAs isolated from ES cells, retrovirus-induced iPS cells (clone 20D-17), plasmid-induced iPS cells (clones 440A-3, -4, -7, -8, -10, and -11 and clone 432A-1), and MEFs were analyzed with RT-PCR. **(E)** Chimeric mice derived from the clone 432A-1. **(F)** Detection of plasmid integration by PCR. Genomic DNA from a C57BL/6 mouse, retrovirus-induced iPS cells (clone 20D-17), plasmid-induced iPS cells (clone 432A-1 and clones 440A-1 to -11), and MEFs were amplified by PCR with primers indicated in (A). In PCR for O-1, K, and M, bands derived from the endogenous (endo) genes are shown with open arrowheads, whereas those from integrated plasmids (Tg) shown with solid arrowheads. For the Fbx15 reporter, the lower bands indicate the wild-type allele, whereas the upper bands indicate the knock-in allele. Minor PCR bands seen in some virus-free clones are smaller than expected and are most likely derived from primer dimers.

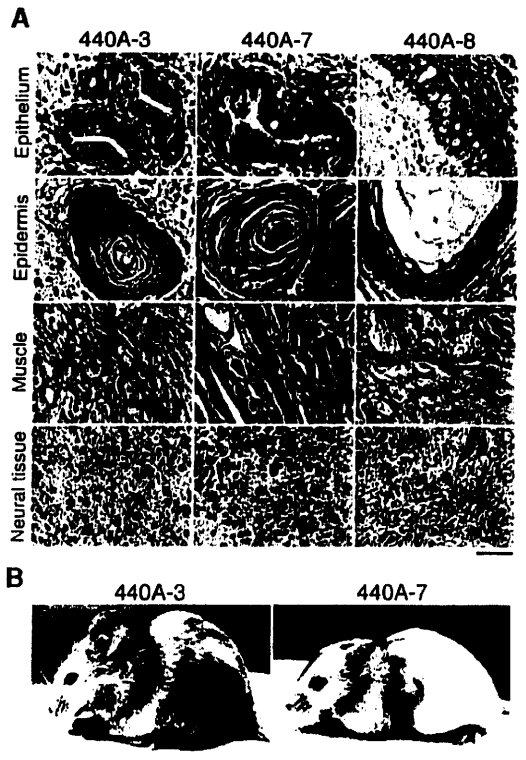

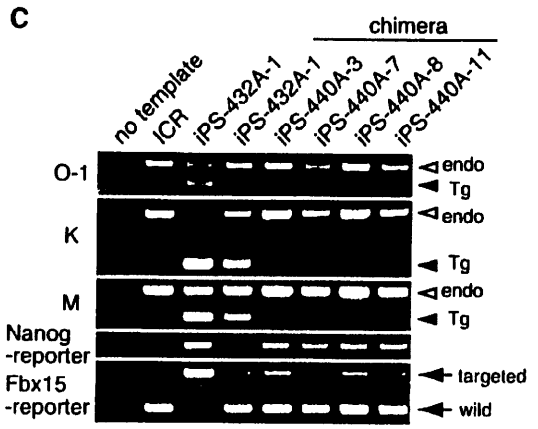

Fig. 3. Pluripotency of virus-free iPS cells without evidence of transgene integration. **(A)** Teratoma formation. Virus-free iPS cells (clones 440A-3, -7, and -8) were subcutaneously transplanted into nude mice. After 4 weeks, tumors were sectioned and stained with hematoxylin and eosin staining. Shown are gutlike epithelial tissues (upper), epidermal tissues, striated muscles, and neural tissues (bottom). Scale bar, 50 μm. **(B)** Chimeric mice derived from virus-free iPS cells (clones 440A-3 and -7). **(C)** Detection of plasmid integration by PCR. Genomic DNA was extracted from an ICR mouse, iPS cells (clone 432A-1), and chimeric mice derived from plasmid-induced iPS cells (clone 432A-1 and clones 440A-3, -7, -8, and -11) and was analyzed with PCR to amplify fragments O-1, K, and M indicated in Fig. 2A. Bands derived from the endogenous genes are shown with open arrowheads, whereas those from integrated plasmids were with solid arrowheads. The presence of the Nanog reporter and the Fbx15 reporter was also detected by PCR.

440, we used MEFs derived from five mouse embryos. SSLP analyses were able to distinguish these five and identified the origin of each virus-free iPS cells. The analyses also confirmed that virus-free iPS cells are different from ES cells, the latter of which were derived from the mouse strain 129S4 (fig. S3).

We performed 10 independent experiments with this transfection protocol (table S1). In 7 out of the 10 experiments, we obtained GFP-positive colonies. In these experiments, 1 to 29 GFP-positive colonies emerged from 1×10^6 transfected cells. When we used retroviruses, we routinely obtained >100 GFP-positive colonies with this number of transfected cells when using three factors and ~1000 GFP-positive colonies with the four factors. In addition, because we re-plated transfected MEFs at day 9, some virus-free iPS cell clones may derive from common progenitor cells. Thus, the efficiency of iPS cell induction with the plasmid transfection protocol is substantially lower than that with the retroviral method. Nevertheless, we obtained iPS cell clones without evidence of plasmid integration in 6 out of 10 experiments (figs. S2 to S5), demonstrating reproducibility of the protocol.

To confirm pluripotency of these iPS cells, we transplanted them subcutaneously into nude mice. All clones tested (440A-3, -4, -7, -8, -10, and -11; 492B-4 and -9; 497B-30; and 497D-2) gave rise to tumors containing a wide variety of cell types, including cells derived from all three germ layers (Fig. 3A and fig. S5). We also injected the iPS cells into blastocysts from the mouse strain ICR. From all clones injected (440A-3, -4, -6, -7, -8, -9, -10, and -11; 492B-4 and 9), we obtained adult chimeras, as judged from coat color (Fig. 3B). In these chimera mice, we did not detect integration of the transgenes by PCR (Fig. 3C). Furthermore, PCR analyses detected both the Nanog reporter and the Fbx15 reporter (*20*) in chimeras (Fig. 3C). Because we generated these virus-free iPS cells from the double reporter mice in the experiment number 440 and because we do not have double reporter ES cells in our laboratory, these data confirmed that these chimeras were derived from the virus-free iPS cells but not from contaminated ES cells. These results confirm pluripotency of iPS cells generated by plasmid transfection methods.

We previously reported that we did not find common retroviral integration sites in iPS cell derived from mouse liver and stomach (*13*). The current study shows dispensability of retroviral integration in iPS cell generation. The efficiency of iPS cell generation, however, is substantially lower without retroviruses. This may suggest that retroviral integration facilitates iPS cell generation. Alternatively, the lower efficiency may be attributable to lower transgene expression levels observed with plasmid transfection than those with retroviruses (fig. S6). Further studies are required to increase the efficiency of virus-free iPS cells. In addition, whether virus-free iPS cells are germline-competent and whether they can be generated from adult somatic cells remain to be determined. Nevertheless, our study is an important step toward studying patient-specific cells and associated disease as well as future application of iPS cell technology in regenerative medicine and other clinical usages.

References and Notes

1. K. Takahashi, S. Yamanaka, *Cell* **126**, 663 (2006).
2. W. E. Lowry *et al.*, *Proc. Natl. Acad. Sci. U.S.A.* **105**, 2883 (2008).
3. I. H. Park *et al.*, *Nature* **451**, 141 (2008).
4. K. Takahashi *et al.*, *Cell* **131**, 861 (2007).
5. J. Yu *et al.*, *Science* **318**, 1917 (2007); published online 19 November 2007 (10.1126/science.1151526).
6. N. Maherali *et al.*, *Cell Stem Cell* **1**, 55 (2007).
7. K. Okita, T. Ichisaka, S. Yamanaka, *Nature* **448**, 313 (2007).
8. M. Wernig *et al.*, *Nature* **448**, 318 (2007).
9. M. Nakagawa *et al.*, *Nat. Biotechnol.* **26**, 101 (2008).
10. M. Wernig, A. Meissner, J. P. Cassady, R. Jaenisch, *Cell Stem Cell* **2**, 10 (2008).
11. A. W. Nienhuis, C. E. Dunbar, B. P. Sorrentino, *Mol. Ther.* **13**, 1031 (2006).
12. S. Yamanaka, *Cell Stem Cell* **1**, 39 (2007).
13. T. Aoi *et al.*, *Science* **321**, 699 (2008); published online 12 February 2008 (10.1126/science.1154884).
14. T. Brambrink *et al.*, *Cell Stem Cell* **2**, 151 (2008).
15. M. Stadtfeld, N. Maherali, D. T. Breault, K. Hochedlinger, *Cell Stem Cell* **2**, 230 (2008).
16. E. C. Hsiao *et al.*, *PLoS One* **3**, e2532 (2008).
17. K. Hasegawa, A. B. Cowan, N. Nakatsuji, H. Suemori, *Stem Cells* **25**, 1707 (2007).
18. S. Morita, T. Kojima, T. Kitamura, *Gene Ther.* **7**, 1063 (2000).
19. H. Niwa, K. Yamamura, J. Miyazaki, *Gene* **108**, 193 (1991).
20. Y. Tokuzawa *et al.*, *Mol. Cell. Biol.* **23**, 2699 (2003).

21. We thank K. Takahashi, K. Yae, M. Koyanagi, and K. Tanabe for scientific discussion; K. Okuda, M. Narita, A. Okada, H. Miyachi, S. Kitano, and N. Takizawa for technical assistance; R. Kato, R. Iyama, E. Nishikawa, and Y. Shimazu for administrative assistance; and D. Srivastava for critical reading of the manuscript. We also thank J. Miyazaki for the CAG promoter.